

# Image Plane Modal Identification in Photogrammetric Dynamic Analysis

Gerald Robert Holmes<sup>1</sup>  
B.S. May 1993, Purdue University

A Thesis submitted to  
The Faculty of  
The Graduate School of Engineering and Applied Science  
of The George Washington University in partial satisfaction  
of the requirements for the degree of Master of Science

November 1995

Thesis directed by  
Dr. Robert H. Tolson

<sup>1</sup>This research conducted at NASA LaRC

# Abstract

There is a great interest in developing options for measuring the structural dynamic characteristics of space structures. These measurements are used to improve structural analytical models and modeling techniques and to modify control systems if unexpected dynamics occur. On space structures it is difficult to mount accelerometers on critical appendages(i.e. solar arrays) and to transmit the signals across rotating joints. One alternative to the usual accelerometer approach is the method of photogrammetry.

In photogrammetry, data from several cameras are triangulated to obtain the time series of positions of selected targets in the global 3-dimensional coordinate system. Modal identification is then performed on the time series. A concern regarding this approach is the inclusion of random errors in the data due to each camera. If the errors are not removed the errors become part of the global system and increase the uncertainty of the system identification of the structure.

The Image Plane Modal Analysis (IPMA) identification is presented as a method to assist in the identification of noise modes in the system by analyzing the image plane data before the triangulation is performed. In the new method, system modes identified in the image plane are used to reconstruct target motion in the image plane coordinate system. To evaluate this method a test was performed using the Earth Observing System dynamics testbed, a testbed that emulates the structural dynamics of the EOS-AM1 satellite. The time series of points on the structure were subjected to the IPMA identification method and the results were compared to both the baseline accelerometer data and the standard method of triangulation. Results show improved identification of system modes using the IPMA method over the standard triangulation method.

# Contents

<b>Abstract</b>	<b>i</b>
<b>List of Figures</b>	<b>v</b>
<b>Nomenclature</b>	<b>vi</b>
<b>1 Introduction</b>	<b>1</b>
1.1 Problem Description . . . . .	1
1.2 Background . . . . .	3
<b>2 Formulation of Photogrammetric Methods</b>	<b>6</b>
2.1 Introduction . . . . .	6
2.2 Mathematical Background . . . . .	6
2.2.1 Geometric Principles . . . . .	7
2.2.2 Collinearity Equation . . . . .	9
2.2.3 Triangulation . . . . .	11
2.2.4 Determination of Projective Parameters . . . . .	11
<b>3 Eigensystem Realization Algorithm</b>	<b>17</b>
3.1 Derivation . . . . .	17
3.2 Modal Amplitude Coherence . . . . .	24
<b>4 Technique for Modal Analysis in Image Plane</b>	<b>25</b>
4.1 Image Plane Modal Analysis . . . . .	25
4.2 Items of Concern . . . . .	27

<b>5</b>	<b>EOS-AM Dynamic Test Article</b>	<b>29</b>
5.1	Description . . . . .	29
5.2	Experiment Description . . . . .	31
<b>6</b>	<b>Image Plane Modal Analysis Results</b>	<b>36</b>
6.1	Accelerometer Data System Identification Results . . . . .	36
6.2	Photogrammetric Analysis Results . . . . .	45
6.3	Image Plane Analysis Results . . . . .	50
<b>7</b>	<b>Conclusions</b>	<b>61</b>
<b>A</b>	<b>Partial Derivatives of Collinearity Equations</b>	<b>63</b>
<b>B</b>	<b>Accelerometer Time Series</b>	<b>65</b>
<b>C</b>	<b>Triangulated Targets' Time Series</b>	<b>70</b>
<b>D</b>	<b>Image Plane Targets' Time Series</b>	<b>74</b>

# List of Figures

1.1	Shuttle-Mir Docked Configuration For PASDE Experiment . . . . .	5
2.1	Coordinate System for Photogrammetric Problem . . . . .	8
2.2	Coordinate System for Photogrammetric Problem . . . . .	8
5.1	First Bending Mode of Solar Array Appendage . . . . .	32
5.2	Second Bending Mode of Solar Array Appendage . . . . .	33
5.3	Camera Views of EOS-AM1 Testbed . . . . .	34
6.1	Singular Value Decomposition for Accelerometer Data . . . . .	37
6.2	Modal Amplitude Coherence for Accelerometers vs. No. of Row Shifts	39
6.3	Identification Results at 0.65 Hz, Accelerometer Data . . . . .	42
6.4	Identification Results at 2.6 Hz, Accelerometer Data . . . . .	43
6.5	Identification Results at 5.8 Hz, Accelerometer Data . . . . .	43
6.6	Measured and Reconstructed Free-Decay Data, Accl.# 1 . . . . .	44
6.7	Measured and Reconstructed Free-Decay Data, Accl# 11 . . . . .	44
6.8	Normalized Singular Value Decomposition For Triangulated Data . .	46
6.9	Modal Amplitude Coherence For Triangulated Data . . . . .	47
6.10	Identification Results at 0.65 Hz, Triangulated Data . . . . .	48
6.11	Identification Results at 1.29 Hz, Triangulated Data . . . . .	48
6.12	Identification Results at 0.12 Hz, Triangulated Data . . . . .	49
6.13	Comparison of Actual and Reconstructed Data, Target #1 X Dir. . .	49
6.14	Comparison of Actual and Reconstructed Data, Target #1 Y Dir. . .	50
6.15	Modal Amplitude Coherence for Image Plane 1 . . . . .	52

6.16	Modal Amplitude Coherence for Image Plane 2	53
6.17	Modal Amplitude Coherence for Image Plane 3	54
6.18	Modal Amplitude Coherence for Image Plane 4	55
6.19	Modal Amplitude Coherence for All Image Plane Time Series	57
6.20	Comparison of Actual and Reconstructed Data, Target 4 X Dir.	58
6.21	Modal Amplitude Coherence for Reconstructed Data	59
B.1	Accelerometer Time Series # 1-8	67
B.2	Accelerometer Time Series # 9-16	68
B.3	Accelerometer Time Series # 17-24	69
C.1	Triangulated Time Series # 1-8	71
C.2	Triangulated Time Series # 9-16	72
C.3	Triangulated Time Series # 17-24	73
D.1	Image Plane # 1 Time Series	75
D.2	Image Plane # 2 Time Series	77
D.3	Image Plane # 3 Time Series	79
D.4	Image Plane # 4 Time Series	81

# Nomenclature

## Roman

$A$	Vector from projection center to object point
$A_c(t)$	Continuous state matrix
$a$	Image vector in image coordinate system
$B_{ij}$	Matrix of partial derivative with approximate values
$B_c(t)$	Continuous input matrix
$B_2$	Input influence matrix
$b_{ij}$	Partial derivative with approximate values for orientation parameters
$C_m$	Difference matrix for parameter approximations and measurements
$C_v$	Damping matrix
$C(t)$	Measurement state matrix
$c$	Principle distance
$D(t)$	Direct transmission state matrix
$E_m, E_r$	Selection matrices
$F_1, F_2$	Current iteration values for $f_1$ and $f_2$
$f_i$	Collinear equation
$f(q, t)$	Generalized forcing function
$H(i)$	Hankel matrix
$K$	Stiffness Matrix
$k$	Time step
$M(t)$	Mass matrix
$M$	Rotation matrix in photogrammetric method
$m$	Number of cameras in photogrammetric system
$n$	Number of object points in photogrammetric system

$\mathcal{P}$	Observability matrix
$\partial$	Partial derivative
$q$	Generalized coordinate
$\bar{q}_i$	modal response history
$\mathcal{Q}$	Controllability matrix
$R, \Sigma, S$	Hankel decomposition matrices
$\sigma$	Singular values
$t$	Time
$t_o$	Time at initial conditions
$u(t)$	Input vector
$V_{x_{ij}}$	Correction for random errors in measured values
$(X, Y, Z)$	Object coordinate system
$X_o$	Location of projection center in object space
$x, y, z$	Coordinate in image coordinate system
$x_p, y_p$	Coordinate of perspective center in image coordinate system
$x_t$	Continuous time solution
$\dot{x}(t)$	State vector
$y(t)$	Output state vector
$\Delta t$	Discrete time interval
$r$	Number of inputs
$Y_i$	Markov parameters
$z$	Matrix of eigenvalues

#### Greek

$\Delta$	Corrections for orientation parameters
$\lambda$	Scale factor, Eigenvalues
$\omega, \phi, \kappa$	Rotation of image coordinate system with respect to the object coordinate system
$\omega$	Frequency vector

$\phi$	Eigenvectors
$\zeta$	Damping values

#### Subscripts

$o$	Camera projection center
$j$	Target point being tracked
$p$	Perspective center
$\alpha$	size of observability matrix
$\beta$	size of controllability matrix

#### Superscripts

$\infty$	Measured value
$\circ$	Approximate value
$\cdot$	Interior parameters
$\cdot\cdot$	Exterior parameters

#### Acronyms

CCD	Charge-Coupled Device
EOS-AM1	Earth Observing System Satellite
ERA	Eigensystem Realization Algorithm
IPMA	Image Plane Modal Analysis
ISS	International Space Station
PASDE	Photogrammetric Appendage Structural Dynamics Experiment

I would like to take this opportunity to thank the people who assisted me in writing this thesis. First and foremost, I would like to thank my two advisors, Dr. Robert H. Tolson and Ms. Sharon Welch. Their constant guidance was a great asset as well as their willingness to answer my endless barrage of questions.

I need to thank the PASDE team members for their constant support and assistance. They are: Mike Gilbert, Rich Pappa, Bob Buchan, Zoran Martinovic, and Michelle Garn. There are several people who are responsible for my laboratory experimentation running smoothly. Dr. Kenny Elliott provided valuable guidance in experimentation, and Melzad Jaweed assisted in the actual set up of the experiment.

There are several people who provided assistance in a wide variety of ways. Dave Cox was an endless source of information regarding Matlab, Sun workstations, and LATEX. Thanks Dave. Todd Wetzel, my officemate, was also very helpful in providing me with counsel and assistance. Good luck with the home brew.

At this point I would like to recognize several of my classmates. Ron Weber and I shared a number of classes together and he was very helpful in explaining concepts that seemed incomprehensible. Jeff Lyon and Hung-sheng Chern were very helpful in numerous ways. Pete Holland kept me well informed with regards to a number of issues, but especially Purdue basketball. Thanks guys.

Thank you to the first year students: Deanna Chipman, Geoff Cook, Jay Daniels, Christian Feruholz, Briau Gallo, Terry Johnson, Katherine Karr ( Roll Tide), Melvin Kosanchick, and Scott Ryun. Thanks for all of the good times. I would also like to thank my friends Steve Smith and Paul Wilkin.

And last, but certainly not least, I would like to send special thank you's to two housemates and a good friend. To Doug Nark, thanks for all of the golf, all of the Sammies, introducing me to Toad and listening to all my complaints. To Jon Lawrence, thanks for not letting me be a home body and the help with P.D.E's. And to my good friend Ray Espiritu, thank you for the words of encouragement in all matters and for being from the Sandwich Islands.

# Chapter 1

## Introduction

### 1.1 Problem Description

The identification of the structural dynamic characteristics of space structures is important for several reasons. These reasons include: 1) improve structural analytical models and modeling techniques, 2) modify control systems if unexpected dynamics occur, and 3) monitor structural health using modal parameters [1]. Accelerometers are normally used to measure the vibrations of structures, but certain design characteristics may prevent the placement of accelerometers at key locations, i.e. solar arrays and thermal radiators. An alternative method that can be used is photogrammetry. It is the purpose of this study to develop a new method to be used with the photogrammetric method to increase the accuracy of the system identification of the structure. The Image Plane Modal Analysis (IPMA) method improves the identification of modal parameters by identifying camera noise in the image plane measurements and allows the noise to be filtered from the data before triangulation. Removing the noise from the data leads to reduced uncertainty in identifying the natural frequencies, damping, and mode-shapes of the structure. Photogrammetry is the science of measuring the location of points in images. The motion of a point over time can be determined if a sequence of images is used. In the traditional use of photogrammetry, the location of a point is determined by making measurements

on time-correlated images from several different cameras. First, the location of the point in the image is determined by identifying the center of the target. Once the location of the point is known in at least several images, the location in global space is calculated. By knowing the location, the orientation, and the characteristics of the camera, the point is located by triangulating the information from the cameras. A more thorough explanation of this process is given in Chapter 2. Once the time series of several points is obtained, system identification techniques are applied to extract the modal parameters of the system. In this study the Eigensystem Realization Algorithm is used to determine the dynamic characteristics of the structure. This method is described in Chapter 3.

The IPMA method differs from the traditional method by applying system identification to the data before triangulation. In the traditional approach, the least-squares method is used to determine the location of the point in global space. If there are errors present, the errors are passed on to the triangulated location. The IPMA method assists in removing errors that are particular to the cameras. By analyzing each camera separately, the structural modes will appear consistently in each of the cameras. Noise that is specific to one camera will not appear in other cameras. The system modes are then identified and used to reconstruct the image plane data for each camera. This reconstructed data is used in the triangulation process and the camera peculiar noise is filtered before the global location calculations.

To evaluate the IPMA method, a vibration test was conducted using the Earth Observing System (EOS-AM1) testbed located at the NASA Langley Research Center. The testbed was excited and the free-decay response of the structure was recorded by 4 CCD cameras located around the test article and by accelerometers on the structure. The accelerometers measurements were used as a baseline for comparing the results from the traditional photogrammetric method and the IPMA method. A detailed explanation of the experiment is given in Chapter 5. The results from the experiment are presented in Chapter 6.

## 1.2 Background

The motivation for this study is provided by the structural verification requirements for the International Space Station (ISS) [1]. As part of the risk mitigation for ISS, on-orbit verification of the structural parameters is necessary. The verification of predicted modal parameters assists in the refinement of current finite element models. This in turn control systems and structural dynamics analysis, as well as uncertainty reduction in the design of future space structures [2]. One method proposed for determining the modal parameters of ISS is the use of photogrammetric methods to make vibration measurements [1]. To validate this technology, an experiment will be conducted on a shuttle mission to the Russian Space Station Mir.

A previous experiment used photogrammetry to determine the structural dynamics of space structures and their appendages, the Solar Array Flight Experiment [3]. SAFE consisted in part of dynamic experiments performed on an extendable and retractable solar array. Because of the design of the array, accelerometers and their associated wiring could not be used. Instead, shuttle video cameras were used to track 18 reflective targets placed on the solar cells of the array. The dynamic characteristics of the solar array were determined from tracking the motion of the targets when the solar array was subjected to various types of inputs and allowed to free-decay.

The Photogrammetric Appendage Structural Dynamics Experiment (PASDE) uses photogrammetric measurements of the mated orbiter-Mir configuration to determine the Mir solar array structural mode frequencies, shapes, and damping. The objective of the PASDE is to demonstrate the passive, low-cost photogrammetric measurement techniques for use in the (ISS) solar array structural verification program[1].

The PASDE will be performed during mission STS-74 after the orbiter has docked with the Mir station. The PASDE will measure the Kvant 2 module solar array motion in response to excitations from STS PRCS jets, docking, and day/night thermal transitions. Cameras located in Hitchhiker gas cans in the payload bay will record the motion of the tip and root of the solar array [1]. There are three gas cans, each one containing two cameras, with one camera focused on the tip and one camera focused

on the root of the array. The mated shuttle-Mir configuration and the locations of the gas cans in the shuttle bay are shown in Figure 1.2. The data will be recorded on Hi-8 mm recorders located in the Hitchhiker cans.

The purpose of the PASDE is to verify the use of photogrammetric methods to obtain low-frequency response data and to extract structural mode information from the data. Also, the results from the experiment will be used to verify and update the structural models of the Mir appendages. This will reduce the uncertainty in the prediction of structural loads to known excitation events. The use of photogrammetry will provide a low cost alternative to accelerometers for meeting ISS on-orbit verification requirements.

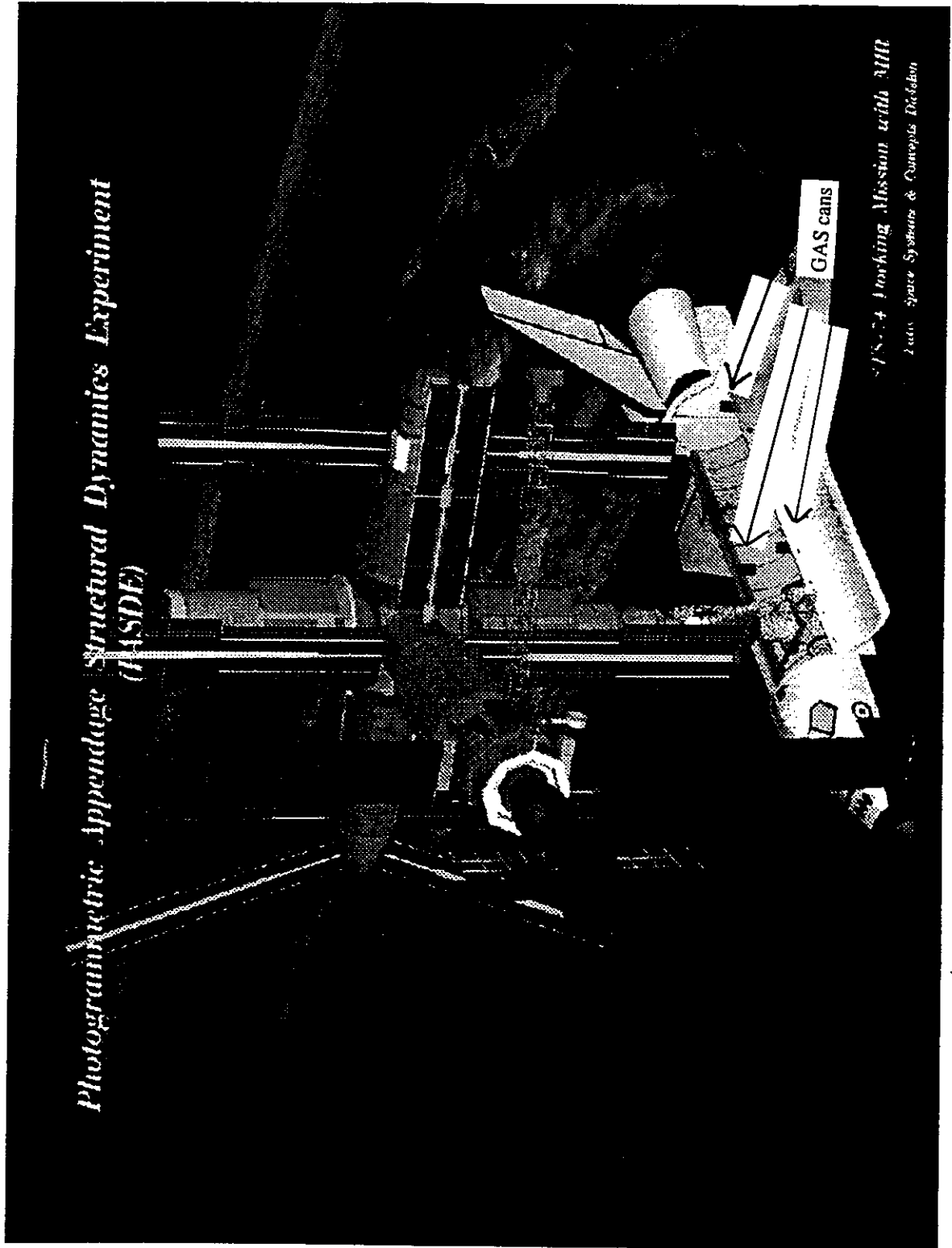


Figure 1.1: Shuttle-Mir Docked Configuration For PASDE Experiment

## **Chapter 2**

# **Formulation of Photogrammetric Methods**

### **2.1 Introduction**

Photogrammetry is defined as making measurements on images [4]. This chapter will first discuss the mathematical principles behind the photogrammetric process, and second, the acquisition of image data. The last part will discuss the calibration techniques used in photogrammetry.

### **2.2 Mathematical Background**

The field of photogrammetry is based on a simple pair of equations known as the collinearity equations. Other names for this pair of equations include the perspective equations, the imaging equations, and the projective equations. These equations relate the two-dimensional location of a point in the image to the three-dimensional location of the point in space. The first step is to describe the orientation of the image system compared to the object space coordinate system. Note that the following discussion relates to both photographic and video images.

## 2.2.1 Geometric Principles

The photogrammetric system consists of the point being imaged, the camera, and the orientation and location of the camera with respect to the point. Figure 2.1 shows the inertial frame  $(X, Y, Z)$  and the camera image coordinate system  $(x, y, z)$  before the rotation of the camera. The origin of the image axes is located at point  $(X_o, Y_o, Z_o)$ , the camera projection center. The point  $j$  is the point being tracked and is located at coordinates  $(X_j, Y_j, Z_j)$ . The image plane is shown a distance  $c$ , the focal length, away from the camera projection center in the negative  $z$  direction.

Figure 2.2 show the same system as presented in Figure 2.1, only the image system has proceeded through three successive rotations about the  $X$ ,  $Y$ , and  $Z$  axes, respectively. Also, the location in the image system of point  $j$ 's image on the image plane is shown, and labeled  $(x, y)$ . The coordinates of the perspective center are  $(x_p, y_p)$ , where the perspective center is defined by the intersection of a line from the projection center to the image plane and the line is normal to the image plane. To accurately define the photogrammetric system, nine parameters need to be defined, the six exterior camera parameters, which are the camera location  $(X_o, Y_o, Z_o)$  and the three rotations for the image system, and the three interior camera parameters,  $x_p, y_p$  and  $c$ .

There are two assumptions made regarding the geometry of the system[5]:

- 1) all images lie in a common plane.
- 2) a point, its image, and the center of projection all lie on a common straight line (the collinearity condition).

The inertial and image plane coordinate systems can be related by successive rotations around the  $X, Y$ , and  $Z$  axes. Defining  $\omega$  as a positive rotation about the  $X$ -axis,  $\phi$  as a positive rotation about the once rotated  $Y$ -axis, and  $\kappa$  as a positive

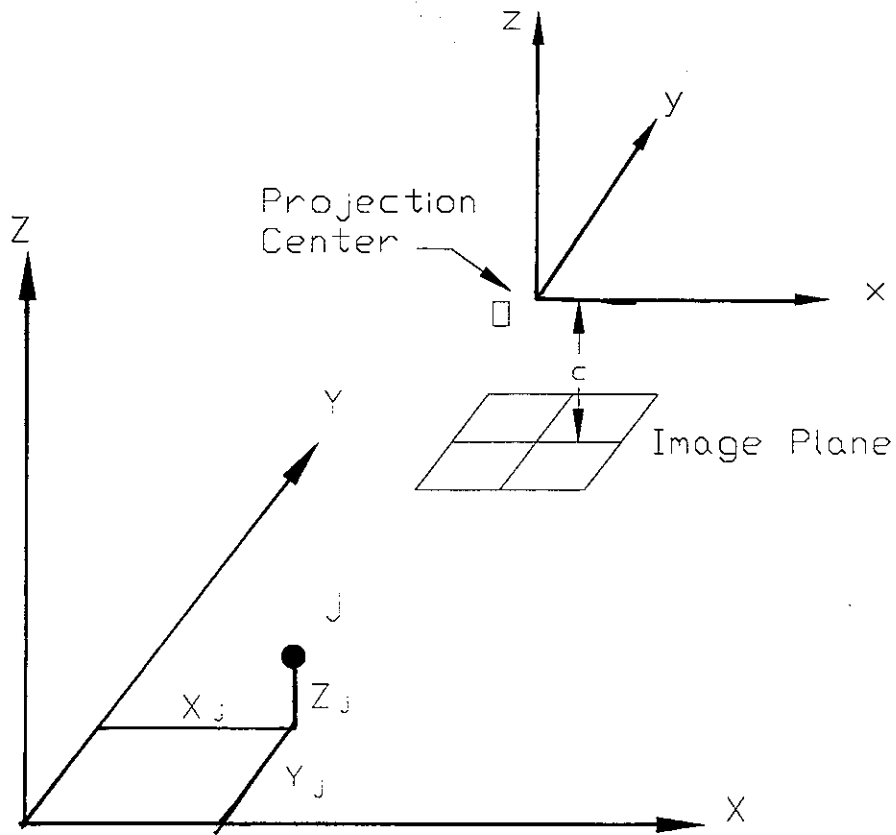


Figure 2.1: Coordinate System for Photogrammetric Problem

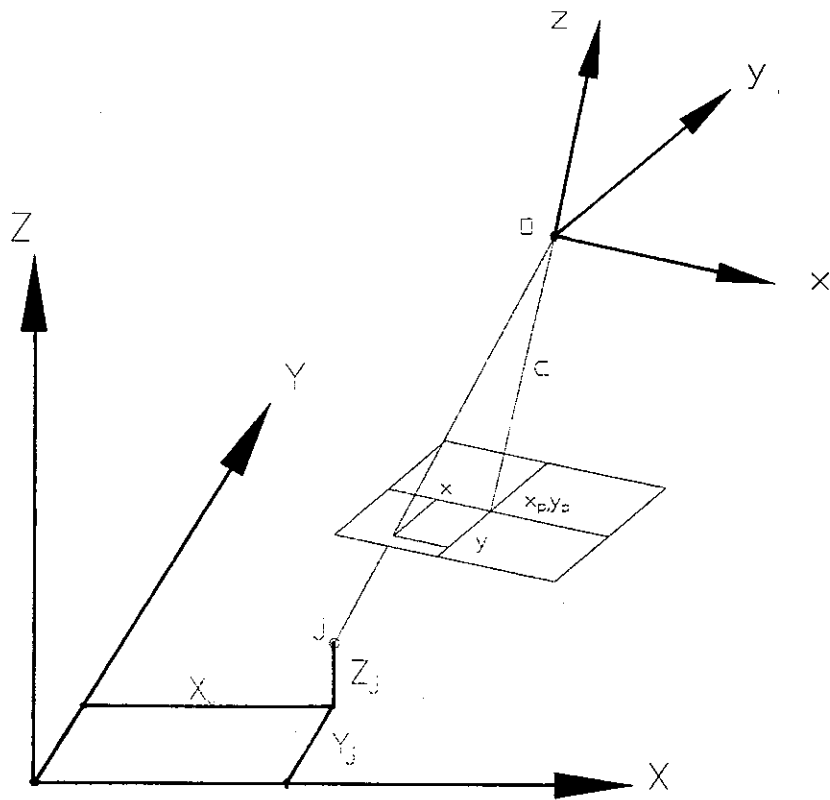


Figure 2.2: Coordinate System for Photogrammetric Problem

rotation about the twice rotated Z-axis gives the rotational matrices

$$\begin{aligned}
 M_\omega &= \begin{bmatrix} 1 & 0 & 0 \\ 0 & \cos \omega & \sin \omega \\ 0 & -\sin \omega & \cos \omega \end{bmatrix} \\
 M_\phi &= \begin{bmatrix} \cos \phi & 0 & -\sin \phi \\ 0 & 1 & 0 \\ \sin \phi & 0 & \cos \phi \end{bmatrix} \\
 M_\kappa &= \begin{bmatrix} \cos \kappa & \sin \kappa & 0 \\ -\sin \kappa & \cos \kappa & 0 \\ 0 & 0 & 1 \end{bmatrix}
 \end{aligned} \tag{2.1}$$

when multiplied sequentially yields

$$M = \begin{bmatrix} \cos \phi \cos \kappa & \sin \omega \sin \phi \cos \kappa + \cos \omega \sin \kappa & -\cos \omega \sin \phi \cos \kappa + \sin \omega \sin \kappa \\ -\cos \phi \sin \kappa & -\sin \omega \sin \phi \sin \kappa + \cos \omega \cos \kappa & \cos \omega \sin \phi \sin \kappa + \sin \omega \cos \kappa \\ \sin \phi & -\sin \omega \cos \phi & \cos \omega \cos \phi \end{bmatrix} \tag{2.2}$$

as the total rotation transition matrix from the  $(X, Y, Z)$  to the  $(x, y, z)$  coordinate system.

### 2.2.2 Collinearity Equation

Matrix  $M$  relates the image coordinate system to the object coordinate system. Defining the image vector in the image coordinate system as

$$a = \begin{bmatrix} x - x_p \\ y - y_p \\ -c \end{bmatrix} \tag{2.3}$$

where  $(x_p, y_p)$  are the coordinates of the perspective center and  $c$  is the principle distance of the lens. Define the vector from the projection center to the object point

as

$$A = \begin{bmatrix} X_j - X_o \\ Y_j - Y_o \\ Z_j - Z_o \end{bmatrix} \quad (2.4)$$

Due to the assumption of collinearity, the image and object rays are collinear and the components of each vector expressed in the same coordinate system are equal except for a scale factor.

Rotating vector  $A$  by the matrix  $M$  and multiplying by the scale factor gives the equation

$$a = \lambda M A$$

$$\begin{bmatrix} x - x_p \\ y - y_p \\ -c \end{bmatrix} = \lambda M \begin{bmatrix} X - X_o \\ Y - Y_o \\ Z - Z_o \end{bmatrix} \quad (2.5)$$

Dividing the first and second equation by the third yields

$$\begin{aligned} \frac{x - x_p}{-c} &= \frac{m_{11}(X - X_o) + m_{12}(Y - Y_o) + m_{13}(Z - Z_o)}{m_{31}(X - X_o) + m_{32}(Y - Y_o) + m_{33}(Z - Z_o)} \\ \frac{y - y_p}{-c} &= \frac{m_{21}(X - X_o) + m_{22}(Y - Y_o) + m_{23}(Z - Z_o)}{m_{31}(X - X_o) + m_{32}(Y - Y_o) + m_{33}(Z - Z_o)} \end{aligned} \quad (2.6)$$

Rearranging gives the most useful forms in terms of two functions

$$\begin{aligned} f_1 &\stackrel{\text{def}}{=} X - X_p + c \frac{m_{11}(X - X_o) + m_{12}(Y - Y_o) + m_{13}(Z - Z_o)}{m_{31}(X - X_o) + m_{32}(Y - Y_o) + m_{33}(Z - Z_o)} = 0 \\ f_2 &\stackrel{\text{def}}{=} Y - Y_p + c \frac{m_{21}(X - X_o) + m_{22}(Y - Y_o) + m_{23}(Z - Z_o)}{m_{31}(X - X_o) + m_{32}(Y - Y_o) + m_{33}(Z - Z_o)} = 0 \end{aligned} \quad (2.7)$$

where  $m_{ij}$  is the  $i, j$  element of  $M$ .

Equation 2.7 are the fundamental equations of photogrammetry and involve nine independent projective parameters [6]

- 1) 3 translations  $X_o, Y_o, Z_o$ .
- 2) 3 translations  $x_p, y_p, c$ .
- 3) 3 parameters  $(\omega, \phi, \kappa)$  which uniquely define the orientation of the image coordinate system with respect to the object coordinate system.

### 2.2.3 Triangulation

Consider a system of  $n$  objects that is photographed from various locations by  $m$  cameras. Assume that the nine projective parameters are perfectly known for the system. Then denote the location of point  $j$  on photo  $i$  by coordinates  $(x_{ij}, y_{ij})$ . Putting these into the collinearity equations yield

$$\begin{aligned} f_{1ij} &= x_{ij} - x_{pi} + c_i \frac{m_{11i}(X_j - X_{oi}) + m_{12i}(Y_j - Y_{oi}) + m_{13i}(Z_j - Z_{oi})}{m_{31i}(X_j - X_{oi}) + m_{32i}(Y_j - Y_{oi}) + m_{33i}(Z_j - Z_{oi})} = 0 \\ f_{2ij} &= y_{ij} - y_{pi} + c_i \frac{m_{21i}(X_j - X_{oi}) + m_{22i}(Y_j - Y_{oi}) + m_{23i}(Z_j - Z_{oi})}{m_{31i}(X_j - X_{oi}) + m_{32i}(Y_j - Y_{oi}) + m_{33i}(Z_j - Z_{oi})} = 0 \end{aligned} \quad (2.8)$$

For point  $j$  on photograph  $i$  there are 2 equations with 3 unknowns  $(X_j, Y_j, Z_j)$ . However, if point  $j$  is examined on all  $m$  photographs, then we have  $2m$  equations and only 3 unknowns. If  $m \geq 2$  then the system is over determined. This allows the application of the method of least squares to improve the accuracy of  $(X_j, Y_j, Z_j)$  [7]. Before the least squares solution can be obtained the non-linear equations must be linearized. The partial derivatives of the collinear equations with respect to each of the parameters and  $x, y$  are given in Appendix A.

### 2.2.4 Determination of Projective Parameters

If the projective parameters are not known, there are several methods for determining the camera rotation angles, the camera positions, and the focal lengths. Two methods will be presented here, the method of photographic resection and the bundle method of photogrammetric triangulation.

#### Bundle Adjustment Method Of Photogrammetric Triangulation

The bundle method simultaneously considers all of the sets of photogrammetric rays (or bundles) from all cameras in an iterative process. If each of the  $n$  points appears in the  $m$  cameras then the full system generates  $2mn$  collinearity equations. The advantage of the bundle method is that it concurrently deals with the photogrammetric resection and triangulation. Therefore the bundle method does not require control points except for the minimum needed for defining a unique coordinate sys-

tem. However, the method can accommodate any control points made available from other surveying methods [5].

The image coordinates are modeled by

$$\begin{aligned}x_{ij} &= x_{ij}^{\circ\circ} + V_{x_{ij}} \\y_{ij} &= y_{ij}^{\circ\circ} + V_{y_{ij}}\end{aligned}\tag{2.9}$$

where  $x_{ij}^{\circ\circ}$  is the measured value (denoted by  $\circ\circ$ ) and  $V_{x_{ij}}$  is the correction for the random errors assumed to be in the system or the measurement. Likewise,

$$\begin{aligned}\omega_i &= \omega_i^{\circ} + \Delta\omega_i & \phi_i &= \phi_i^{\circ} + \Delta\phi_i & \kappa_i &= \kappa_i^{\circ} + \Delta\kappa_i \\X_i^c &= (X_i^c)^{\circ} + \Delta X_i^c & Y_i^c &= (Y_i^c)^{\circ} + \Delta Y_i^c & Z_i^c &= (Z_i^c)^{\circ} + \Delta Z_i^c \\X_j &= X_j^{\circ} + \Delta X_j & Y_j &= Y_j^{\circ} + \Delta Y_j & Z_j &= Z_j^{\circ} + \Delta Z_j\end{aligned}\tag{2.10}$$

$\omega_i^{\circ} \dots Z_j^{\circ}$  are approximations (denoted by  $\circ$ ) and  $\Delta\omega_i \dots \Delta Z_j$  are their corresponding corrections. Using the linearizations presented in Appendix A, the Taylor first order approximations can be written as

$$\begin{aligned}V_{x_{ij}} &+ \left(\frac{\partial F_x}{\partial \omega_i}\right)^{\circ} \Delta\omega_i + \left(\frac{\partial F_x}{\partial \phi_i}\right)^{\circ} \Delta\phi_i + \left(\frac{\partial F_x}{\partial \kappa_i}\right)^{\circ} \Delta\kappa_i + \left(\frac{\partial F_x}{\partial X_i^c}\right)^{\circ} \Delta X_i^c + \left(\frac{\partial F_x}{\partial Y_i^c}\right)^{\circ} \Delta Y_i^c + \left(\frac{\partial F_x}{\partial Z_i^c}\right)^{\circ} \Delta Z_i^c + \\&\left(\frac{\partial F_x}{\partial x_{pi}}\right)^{\circ} \Delta x_{pi} + \left(\frac{\partial F_x}{\partial y_{pi}}\right)^{\circ} \Delta y_{pi} + \left(\frac{\partial F_x}{\partial c_i}\right)^{\circ} \Delta c_i + \left(\frac{\partial F_x}{\partial X_j}\right)^{\circ} \Delta X_j + \left(\frac{\partial F_x}{\partial Y_j}\right)^{\circ} \Delta Y_j + \left(\frac{\partial F_x}{\partial Z_j}\right)^{\circ} \Delta Z_j + F_x^{\circ} = 0 \\V_{y_{ij}} &+ \left(\frac{\partial F_y}{\partial \omega_i}\right)^{\circ} \Delta\omega_i + \left(\frac{\partial F_y}{\partial \phi_i}\right)^{\circ} \Delta\phi_i + \left(\frac{\partial F_y}{\partial \kappa_i}\right)^{\circ} \Delta\kappa_i + \left(\frac{\partial F_y}{\partial X_i^c}\right)^{\circ} \Delta X_i^c + \left(\frac{\partial F_y}{\partial Y_i^c}\right)^{\circ} \Delta Y_i^c + \left(\frac{\partial F_y}{\partial Z_i^c}\right)^{\circ} \Delta Z_i^c + \\&\left(\frac{\partial F_y}{\partial x_{pi}}\right)^{\circ} \Delta x_{pi} + \left(\frac{\partial F_y}{\partial y_{pi}}\right)^{\circ} \Delta y_{pi} + \left(\frac{\partial F_y}{\partial c_i}\right)^{\circ} \Delta c_i + \left(\frac{\partial F_y}{\partial X_j}\right)^{\circ} \Delta X_j + \left(\frac{\partial F_y}{\partial Y_j}\right)^{\circ} \Delta Y_j + \left(\frac{\partial F_y}{\partial Z_j}\right)^{\circ} \Delta Z_j + F_y^{\circ} = 0\end{aligned}\tag{2.11}$$

where  $F_x^{\circ}$  is  $f_1$  and  $F_y^{\circ}$  is  $f_2$  calculated with the current iteration values for the

parameters [8]. Let

$$\begin{aligned}
b_{11} &= \left(\frac{\partial F_x}{\partial \omega_i}\right)^\circ & b_{21} &= \left(\frac{\partial F_y}{\partial \omega_i}\right)^\circ \\
b_{12} &= \left(\frac{\partial F_x}{\partial \phi_i}\right)^\circ & b_{22} &= \left(\frac{\partial F_y}{\partial \phi_i}\right)^\circ \\
b_{13} &= \left(\frac{\partial F_x}{\partial \kappa_i}\right)^\circ & b_{23} &= \left(\frac{\partial F_y}{\partial \kappa_i}\right)^\circ \\
b_{14} &= \left(\frac{\partial F_x}{\partial X_i^c}\right)^\circ & b_{24} &= \left(\frac{\partial F_y}{\partial X_i^c}\right)^\circ \\
b_{15} &= \left(\frac{\partial F_x}{\partial Y_i^c}\right)^\circ & b_{25} &= \left(\frac{\partial F_y}{\partial Y_i^c}\right)^\circ \\
b_{16} &= \left(\frac{\partial F_x}{\partial Z_i^c}\right)^\circ & b_{26} &= \left(\frac{\partial F_y}{\partial Z_i^c}\right)^\circ \\
b_{17} &= \left(\frac{\partial F_x}{\partial x_{pi}}\right)^\circ & b_{27} &= \left(\frac{\partial F_y}{\partial x_{pi}}\right)^\circ \\
b_{18} &= \left(\frac{\partial F_x}{\partial y_{pi}}\right)^\circ & b_{28} &= \left(\frac{\partial F_y}{\partial y_{pi}}\right)^\circ \\
b_{19} &= \left(\frac{\partial F_x}{\partial c_i}\right)^\circ & b_{29} &= \left(\frac{\partial F_y}{\partial c_i}\right)^\circ \\
b_{110} &= \left(\frac{\partial F_x}{\partial X_j}\right)^\circ & b_{210} &= \left(\frac{\partial F_y}{\partial X_j}\right)^\circ \\
b_{111} &= \left(\frac{\partial F_x}{\partial Y_j}\right)^\circ & b_{211} &= \left(\frac{\partial F_y}{\partial Y_j}\right)^\circ \\
b_{112} &= \left(\frac{\partial F_x}{\partial Z_j}\right)^\circ & b_{212} &= \left(\frac{\partial F_y}{\partial Z_j}\right)^\circ
\end{aligned} \tag{2.12}$$

Then 2.11 can be written as

$$V_{ij} + \dot{B}_{ij}\dot{\Delta}_i + \ddot{B}_{ij}\ddot{\Delta}_i = \epsilon_{ij} \tag{2.13}$$

where  $\dot{B}_{ij}$  is the first nine columns of matrix  $b$  and  $\ddot{B}_{ij}$  is the last three columns of matrix  $b$ . Also,  $\epsilon_{ij}$  is  $F_x^\circ$  and  $F_y^\circ$ ,  $V_{ij}$  is a column vector consisting of  $V_{x_{ij}}$  and  $V_{y_{ij}}$ , and  $\Delta_i$  are the corrections for the appropriate parameters.

If  $X_j^{\circ\circ}, Y_j^{\circ\circ}, Z_j^{\circ\circ}$  are measured values for control point  $j$ , then the coordinates of the point in object space can be represented by

$$\begin{aligned}
X_j &= X_j^{\circ\circ} + V_{X_j} \\
Y_j &= Y_j^{\circ\circ} + V_{Y_j} \\
Z_j &= Z_j^{\circ\circ} + V_{Z_j}
\end{aligned} \tag{2.14}$$

Combining 2.15 with 2.10 and rearranging yields

$$\begin{bmatrix} V_{X_j} \\ V_{Y_j} \\ V_{Z_j} \end{bmatrix} - \begin{bmatrix} \Delta X_j \\ \Delta Y_j \\ \Delta Z_j \end{bmatrix} = \begin{bmatrix} X_j^\circ - X_j^{\circ\circ} \\ Y_j^\circ - Y_j^{\circ\circ} \\ Z_j^\circ - Z_j^{\circ\circ} \end{bmatrix} \tag{2.15}$$

or

$$\ddot{V}_j - \ddot{\Delta}_j = \ddot{C}_j \tag{2.16}$$

As with the object space coordinates, observation equations for the external camera parameters can be written. Let  $\omega_i^{\circ\circ} \dots (c_i)^{\circ\circ}$  represent measured values for the external parameters and  $V_{\omega_i} \dots V_{c_i}$  be their corresponding residuals. Thus the true values are given by:

$$\begin{aligned}
\omega_i &= \omega_i^{\circ\circ} + V_{\omega_i} \\
\phi_i &= \phi_i^{\circ\circ} + V_{\phi_i} \\
\kappa_i &= \kappa_i^{\circ\circ} + V_{\kappa_i} \\
X_i^c &= (X_i^c)^{\circ\circ} + V_{X_i^c} \\
Y_i^c &= (Y_i^c)^{\circ\circ} + V_{Y_i^c} \\
Z_i^c &= (Z_i^c)^{\circ\circ} + V_{Z_i^c} \\
x_{pi} &= (x_{pi})^{\circ\circ} + V_{x_{pi}} \\
y_{pi} &= (y_{pi})^{\circ\circ} + V_{y_{pi}} \\
c_i &= (c_i)^{\circ\circ} + V_{c_i}
\end{aligned} \tag{2.17}$$

Combining the previous equation with 2.10 and rearranging gives

$$\begin{bmatrix} V_{\omega_i} \\ V_{\phi_i} \\ V_{\kappa_i} \\ V_{X_i^c} \\ V_{Y_i^c} \\ V_{Z_i^c} \\ V_{x_{pi}} \\ V_{y_{pi}} \\ V_{c_i} \end{bmatrix} - \begin{bmatrix} \Delta\omega_i \\ \Delta\phi_i \\ \Delta\kappa_i \\ \Delta X_i^c \\ \Delta Y_i^c \\ \Delta Z_i^c \\ \Delta x_{pi} \\ \Delta y_{pi} \\ \Delta c_i \end{bmatrix} = \begin{bmatrix} \omega_i^{\circ} - \omega_i^{\circ\circ} \\ \phi_i^{\circ} - \phi_i^{\circ\circ} \\ \kappa_i^{\circ} - \kappa_i^{\circ\circ} \\ (X_i^c)^{\circ} - (X_i^c)^{\circ\circ} \\ (Y_i^c)^{\circ} - (Y_i^c)^{\circ\circ} \\ (Z_i^c)^{\circ} - (Z_i^c)^{\circ\circ} \\ (x_{pi})^{\circ} - (x_{pi})^{\circ\circ} \\ (y_{pi})^{\circ} - (y_{pi})^{\circ\circ} \\ (c_i)^{\circ} - (c_i)^{\circ\circ} \end{bmatrix} \tag{2.18}$$

or

$$\hat{V}_i - \hat{\Delta}_i = \hat{C}_i \tag{2.19}$$

These equations define the exterior parameters for camera  $i$ . It is important to note that observation equations need only be written for those parameters that have measured values[6]. Therefore not all 9 equations need to be included in 2.19.

If point  $j$  appears in all  $m$  cameras then the complete set of collinearity equations

for point  $j$  are

$$V_j + \dot{B}_j \dot{\Delta}_j + \ddot{B}_j \ddot{\Delta}_j = \epsilon_j \quad (2.20)$$

If the collinearity equations are written for all  $n$  points the complete collection is given by

$$V + \dot{B}\dot{\Delta} + \ddot{B}\ddot{\Delta} = \epsilon \quad (2.21)$$

where  $V$  is  $(2mn, 1)$ ,  $\dot{B}$  is  $(2mn, 9m)$ ,  $\dot{\Delta}$  is  $(9m, 1)$ ,  $\ddot{B}$  is  $(2mn, 3n)$ ,  $\ddot{\Delta}$  is  $(3n, 1)$ , and  $\epsilon$  is  $(2mn, 1)$ . To complete the mathematical model of the photogrammetric problem, the observation equations for the exterior orientation parameters and control points need to be added. Assuming all the exterior parameters have been measured, the observation equations for all  $m$  cameras can be combined to give

$$\begin{bmatrix} \dot{V}_1 \\ \dot{V}_2 \\ \vdots \\ \dot{V}_m \end{bmatrix} - \begin{bmatrix} \dot{\Delta}_1 \\ \dot{\Delta}_2 \\ \vdots \\ \dot{\Delta}_m \end{bmatrix} = \begin{bmatrix} \dot{C}_1 \\ \dot{C}_2 \\ \vdots \\ \dot{C}_m \end{bmatrix} \quad (2.22)$$

or

$$\dot{V} - \dot{\Delta} = \dot{C} \quad (2.23)$$

Likewise, for the ground control points the complete set of observation equations is

$$\begin{bmatrix} \ddot{V}_1 \\ \ddot{V}_2 \\ \vdots \\ \ddot{V}_n \end{bmatrix} - \begin{bmatrix} \ddot{\Delta}_1 \\ \ddot{\Delta}_2 \\ \vdots \\ \ddot{\Delta}_n \end{bmatrix} = \begin{bmatrix} \ddot{C}_1 \\ \ddot{C}_2 \\ \vdots \\ \ddot{C}_n \end{bmatrix} \quad (2.24)$$

or

$$\ddot{V} - \ddot{\Delta} = \ddot{C} \quad (2.25)$$

Combining 2.21, 2.23, and 2.25 gives the complete mathematical model of the photogrammetric problem. Putting this into matrix form yields

$$\begin{bmatrix} V \\ \dot{V} \\ \ddot{V} \end{bmatrix} + \begin{bmatrix} \dot{B} & \ddot{B} \\ -I & 0 \\ 0 & -I \end{bmatrix} = \begin{bmatrix} \epsilon \\ \dot{C} \\ \ddot{C} \end{bmatrix} \quad (2.26)$$

or

$$\bar{V} + \bar{B}\Delta = \bar{C} \quad (2.27)$$

The least squares solution for this model results in the following normal equation:

$$(\bar{B}^T \bar{W} \bar{B})\Delta = \bar{B}^T \bar{W} \bar{C} \quad (2.28)$$

where  $\bar{W}$  is the weight matrix. The least-squares solution will be

$$\Delta = (\bar{B}^T \bar{W} \bar{B})^{-1} \bar{B}^T \bar{W} \bar{C} \quad (2.29)$$

The weight matrix is a series of submatrices assigned to the observed parameters. The weight of an observation is inversely proportional to the population variance of the measurement[6]. The weight matrix must be stacked and organized in the same manner as the V-matrix. The weight matrix has the form:

$$\bar{W} = \begin{bmatrix} W & 0 & 0 \\ 0 & \dot{W} & 0 \\ 0 & 0 & \ddot{W} \end{bmatrix} \quad (2.30)$$

where  $W$  is a  $(2mn, 2mn)$  matrix for all  $n$  image coordinates on all  $m$  images,  $\dot{W}$  is a  $(9m, 9m)$  matrix for the 9 camera parameters for all  $m$  cameras, and  $\ddot{W}$  is the  $(3n, 3n)$  weight matrix for the  $n$  control points.

## Chapter 3

# Eigensystem Realization Algorithm

### 3.1 Derivation

Except where noted, most of the following derivation is taken from Juang[9]. To describe the motion of a linear-dynamic system, a set of  $n$  second-order differential equations can be written, where  $n$  is the number of independent coordinates. Letting  $M$ ,  $C_v$ , and  $K$  represent the mass, damping and stiffness matrices of the system, respectively, allows the second order state equations to be written as

$$M(t)\ddot{q} + C_v(t)\dot{q} + K(t)q = f(t) \quad (3.1)$$

where  $\ddot{q}$ ,  $\dot{q}$ ,  $q$  are the vectors of generalized acceleration, velocity, and displacement, respectively, and  $f(q, t)$  is the generalized forcing function applied at certain specific locations. 3.1 can be rewritten using the following definitions:

$$A_c(t) = \begin{bmatrix} 0 & I \\ -M(t)^{-1}K(t) & -M(t)^{-1}C_v(t) \end{bmatrix}, \quad x(t) = \begin{bmatrix} q(t) \\ \dot{q}(t) \end{bmatrix} \quad (3.2)$$
$$B_c(t) = \begin{bmatrix} 0 \\ M(t)^{-1}B_2 \end{bmatrix}, \quad f(q(t), t) = B_2u(t)$$

where  $A_c(t)$  is a  $2n$  by  $2n$  state matrix and  $B_2$  is an  $n$  by  $r$  input influence matrix defining the location and type of inputs. The integer  $r$  is the number of inputs.  $A_c(t)$

and  $B_c(t)$  are continuous time matrices. Thus, 3.1 can be rewritten in first ordered form as

$$\dot{x}(t) = A_c(t)x(t) + B_c(t)u(t) \quad (3.3)$$

The output is defined by the equation

$$y(t) = C(t)x(t) + D(t)u(t) \quad (3.4)$$

where  $C(t)$  is the measurement matrix that selects the proper terms from the state vector  $x(t)$  and  $D(t)$  is the direct transmission matrix that transfers the input directly into the output.

Together 3.3 and 3.4 are the state-variable equations in continuous time. If the system is time-invariant,  $A_c(t)$ ,  $B_c(t)$ ,  $C(t)$  and  $D(t)$  are constant with respect to time and a solution can be found of the form

$$x(t) = e^{A_c(t-t_o)}x(t_o) + \int_{t_o}^t e^{A_c(t-\tau)}B_c u(\tau)d\tau \quad (3.5)$$

where  $x(t_o)$  is the initial conditions at some  $t = t_o$  [10].

This equation describes the variation of state variable  $x$  relative to initial conditions  $x(t_o)$  and input  $u(t)$  for  $t > t_o$ . Since most data is in digital form and is measured at discrete time intervals only, let  $t$  be represented by discrete time intervals  $0, \Delta t, 2\Delta t, \dots, (k+1)\Delta t, \dots$  where  $\Delta t$  is a constant. In 3.5 letting  $t = (k+1)\Delta t$  and  $t_o = k\Delta t$  yields

$$x[(k+1)\Delta t] = e^{A_c(\Delta t)}x(k\Delta t) + \int_{k\Delta t}^{(k+1)\Delta t} e^{A_c((k+1)\Delta t-\tau)}B_c u(\tau)d\tau \quad (3.6)$$

assuming  $u(\tau)$  is constant over the sample interval. Eq. 3.6 becomes

$$x[(k+1)\Delta t] = e^{A_c(\Delta t)}x(k\Delta t) + \left[ \int_0^{\Delta t} e^{A_c(\tau')}d\tau' B_c \right] u(k\Delta t) \quad (3.7)$$

where  $\tau$  has been replaced by  $\tau' = (k+1)\Delta t - \tau$ . If we define

$$\begin{aligned} A &= e^{A_c \Delta t} \\ B &= \int_0^{\Delta t} e^{A_c \tau'} d\tau' B_c \\ x(k+1) &= x[(k+1)\Delta t] \\ u(k) &= u(k\Delta t) \end{aligned} \quad (3.8)$$

Then Eq. 3.7 becomes

$$x(k+1) = Ax(k) + Bu(k) \quad k = 0, 1, 2, \dots \quad (3.9)$$

and Eq. 3.4 becomes

$$y(k) = Cx(k) + Du(k) \quad (3.10)$$

3.9 and 3.10 represent a discrete-time state-space model of a dynamical system. This set of equations forms the basis of system identification of linear, time-invariant, dynamic systems.

Because of the nature of experimental data and the likelihood it will be recorded in digital format, these equations are well suited to describe the system. Matrices  $A, B, C,$  and  $D$  describe the input-output relationship through a discrete-time state vector  $x$ . Given a series of inputs  $u(k) (k = 0, 1, 2, \dots)$  where it is assumed  $u(k)$  is a constant over the sample interval  $k - 1 < k < k + 1$  and an initial condition  $x(t_0)$ , Eqs. 3.9 and 3.10 produce a series of outputs  $y(k) (k = 0, 1, 2, \dots)$  [11].

Solving for  $y(k)$  with zero initial conditions and previous inputs  $u(i) (i = 0, 1, 2, \dots, k)$  yields

$$\begin{aligned} x(0) &= 0 \\ x(1) &= Bu(0) \\ x(2) &= ABu(0) + Bu(1) \\ &\vdots \\ x(k) &= \sum_{i=1}^k A^{i-1} Bu(k-i) \end{aligned} \quad (3.11)$$

$$\begin{aligned} y(0) &= Du(0) \\ y(1) &= CBu(0) + Du(1) \\ y(2) &= CABu(0) + CBu(1) + Du(2) \\ &\vdots \\ y(k) &= \sum_{i=1}^k CA^{i-1} Bu(k-i) + Du(k) \end{aligned} \quad (3.12)$$

If  $u(i)$  is allowed to represent a pulse in one of the input variables  $u_i(0) = 1, (i = 1, 2, \dots, r)$  and  $u_i(k) = 0 (k = 1, 2, \dots)$  the unit pulse response can be determined by substituting into Eqs. 3.11 and 3.12 to yield

$$y(k) = \sum_{i=0}^k Y_{k-1} u_i \quad (3.13)$$

where

$$\begin{aligned}
 Y_0 &= D, \\
 Y_1 &= CB, \\
 Y_2 &= CAB, \\
 &\vdots, \\
 Y_k &= CA^{k-1}B
 \end{aligned}
 \tag{3.14}$$

The constant matrices in the sequence are known as the Markov parameters. Since the Markov parameters are the pulse response of the system, they must be unique for a given system. Therefore determining the Markov parameters from experimental data can be used as the basis for identifying the discrete time models, Eqs. 3.9 and 3.10, represented by the constant matrices  $A, B, C$  and  $D$ . Since  $D = Y_0$ , only the three matrices  $A, B$  and  $C$  need to be determined.

A realization is the computation of a triplet  $[A, B, C]$  from the Markov parameters shown in Eq. 3.14. Any system has an infinite number of realizations that will predict the identical response for a particular input. A minimum realization is one with the smallest state-space dimensions among all realizable systems that have the same input-output relations. All minimum realizations have the same set of eigenvalues, which are modal parameters of the system itself.

The process of system realization begins with the formulation of the generalized Hankel matrix. Its size is  $\alpha m \times \beta r$ , where  $\alpha$  and  $\beta$  are arbitrary integers, and is composed of the Markov parameters

$$H(k-1) = \begin{bmatrix} Y_k & Y_{k+1} & \cdots & Y_{k+\beta-1} \\ Y_{k+1} & Y_{k+2} & \cdots & Y_{k+\beta} \\ \vdots & \vdots & \ddots & \vdots \\ Y_{k+\alpha-1} & Y_{k+\alpha} & \cdots & Y_{k+\alpha+\beta-2} \end{bmatrix}
 \tag{3.15}$$

Recall that  $r$  is the number of inputs and  $m$  is the number of outputs. In theory, if  $\alpha \geq n$  and  $\beta \geq n$  (the order of the system), the matrix  $H(k-1)$  is of rank  $n$ . However,  $H(k-1)$  is usually of full rank due to noise [10]. Substituting the Markov parameters into Eq. 3.15 and decomposing  $H(k-1)$  into three matrices yields

$$H(k-1) = \mathcal{P}_\alpha A^{k-1} \mathcal{Q}_\beta
 \tag{3.16}$$

where  $\mathcal{P}_\alpha$  and  $\mathcal{Q}_\beta$  are

$$\mathcal{P}_\alpha = \begin{bmatrix} C \\ CA \\ CA^2 \\ \vdots \\ CA^{\alpha-1} \end{bmatrix} \quad (3.17)$$

$$\mathcal{Q}_\beta = \begin{bmatrix} B & AB & A^2B & \dots & A^{\beta-1}B \end{bmatrix}$$

Block matrix  $\mathcal{P}_\alpha$  is the observability matrix and  $\mathcal{Q}_\beta$  is the controllability matrix.

The ERA algorithm begins by forming a block data matrix obtained by deleting some rows and columns of the generalized Hankel matrix but keeps the first block matrix intact. i.e.,  $Y_k$ . Also, the standard ordering of entries in generalized Hankel matrix does not need to be maintained.

To determine which rows and columns to delete from the Hankel matrix the singular value decomposition (SVD) is used. This method permits the analyst to select the rank of a matrix based on singular values. In theory, the rank is taken as the number of non-zero singular values. However, all singular values will be non-zero due to noise present in the measurements. In this case, determining which values to keep is typically done by keeping all singular values above a prescribed tolerance or choosing where there is a sudden change in slope of successive singular values. By choosing the rank in this manner, it is assumed that the strong modes are the only ones represented in the system. The rest are considered weakly excited modes or noise modes and disregarded.

The Hankel matrix for  $k = 1$  is decomposed as follows

$$H(0)_{\alpha m \times \beta r} = R_{\alpha m \times \alpha m} \Sigma_{\alpha m \times \beta r} S_{\beta r \times \beta r}^T \quad (3.18)$$

where the columns of  $R$  and  $S$  are orthonormal and  $\Sigma$  is a rectangular matrix

$$\Sigma = \begin{bmatrix} \Sigma_n & 0 \\ 0 & 0 \end{bmatrix} \quad (3.19)$$

where

$$\Sigma_n = \text{diag}[\sigma_1, \sigma_2, \dots, \sigma_i, \sigma_{i+1}, \dots, \sigma_n] \quad (3.20)$$

with

$$\sigma_1 \geq \sigma_2 \geq \dots \geq \sigma_i \geq \sigma_{i+1} \geq \dots \sigma_n \geq 0 \quad (3.21)$$

In practice, only the first  $2n$  modes are selected because they are assumed to be the only true modes of the system while the other modes are noise. Let  $R_n$  and  $S_n$  be the matrices formed by the first  $n$  columns of  $R$  and  $S$ , respectively. Thus, the matrix  $H(0)$  become

$$H(0) = R_n \Sigma_n S_n^T \quad (3.22)$$

Equating 3.16 and 3.22 , with  $k = 1$ ,

$$R_n \Sigma_n S_n^T = \mathcal{P}_\alpha \mathcal{Q}_\beta \quad (3.23)$$

According to Juang [12] the best way to partition 3.23 is the internally balanced form because it is slightly better conditioned than other partition forms. Doing this gives

$$\begin{aligned} \mathcal{P}_\alpha &= R_n \Sigma_n^{1/2} \\ \mathcal{Q}_\alpha &= \Sigma_n^{1/2} S_n^T \end{aligned} \quad (3.24)$$

From 3.17 and 3.24 we have

$$\begin{aligned} C &= E_m \mathcal{P} = E_m R_n \Sigma_n^{1/2} \\ B &= \mathcal{Q} E_r = \Sigma_n^{1/2} S_n^T E_r \end{aligned} \quad (3.25)$$

where  $E_m$  and  $E_r$  are selection matrices denoted by

$$\begin{aligned} E_m &= \begin{bmatrix} I_m & 0_m & 0_m & \dots & 0_m \end{bmatrix} \\ E_r &= \begin{bmatrix} I_r \\ 0_r \\ 0_r \\ \vdots \\ 0_r \end{bmatrix} \end{aligned} \quad (3.26)$$

It should be noted that  $E_m$  and  $E_r$  are never used numerically.

Using 3.16 with  $k = 2$  yields

$$H(1) = \mathcal{P}A\mathcal{Q} \quad (3.27)$$

Since  $\mathcal{P}$  is full row rank and  $\mathcal{Q}$  is full column rank

$$A = (\mathcal{P}^T\mathcal{P})^{-1}\mathcal{P}^T H(1)\mathcal{Q}^T(\mathcal{Q}\mathcal{Q}^T)^{-1} \quad (3.28)$$

Using the orthogonality of  $\mathcal{P}$  and  $\mathcal{Q}$

$$\begin{aligned} (\mathcal{P}^T\mathcal{P})^{-1}\mathcal{P}^T &= (\Sigma_n^T R_n^T R_n \Sigma_n^{1/2})^{-1} \Sigma^{1/2} R^T = \Sigma_n^{-1/2} R_n^T \\ \mathcal{Q}^T(\mathcal{Q}\mathcal{Q}^T)^{-1} &= S_n \Sigma^{1/2} (\Sigma_n^{1/2} S_n^T S_n \Sigma_n^{1/2})^{-1} = S_n \Sigma_n^{-1/2} \end{aligned} \quad (3.29)$$

Therefore

$$A = \Sigma^{-1/2} R_n^T H(1) S_n \Sigma^{-1/2} \quad (3.30)$$

and a minimum realization (of order  $n$ ) is defined by

$$\begin{aligned} C &= E_m R \Sigma^{1/2} \\ A &= \Sigma^{1/2} R^T H(1) S_n \Sigma^{-1/2} \\ B &= \Sigma^{1/2} S_n^T E_r \end{aligned} \quad (3.31)$$

An eigendecomposition of the discrete matrix  $A$  such that

$$A\phi = \phi z \quad (3.32)$$

where  $z$  is a matrix with the eigenvalues of  $A$  along the diagonal and  $\phi$  is the matrix with the eigenvectors corresponding to the eigenvalues in  $z$ . The eigenvalues are transformed to continuous time space by

$$\lambda_i = \frac{\ln(z_i)}{\Delta t} \quad i = 1, \dots, n \quad (3.33)$$

The system natural frequency and damping are

$$\begin{aligned} \omega_{n_i} &= |\lambda_i| \\ \zeta_i &= \frac{-\Re(\lambda_i)}{\omega_{n_i}} \end{aligned} \quad (3.34)$$

where  $||$  denotes magnitude and  $\Re$  indicates the real part of the complex number. The output mode shapes are determined from  $C\phi$  and the modal participation factors are determined from  $\phi^{-1}B$  [10]. It can be shown that the free response data and pulse response data have Hankel matrices of the same form, therefore free response data can be used as well.

The computational steps for the ERA are:

- 1) Obtain pulse response or free-decay data.
- 2) Form Hankel matrices  $H(0)$  and  $H(1)$ .
- 3) Perform the SVD on  $H(0)$  and truncate keeping only the significant modes.
- 4) Compute  $\{A, B, C, D\}$ . If using pulse-response data,  $D$  is obtained from  $r$  columns of  $Y$  matrix. If using free decay,  $D$  does not exist.

### 3.2 Modal Amplitude Coherence

The modal amplitude coherence is one of many indicators developed to quantitatively distinguish between system and noise modes. The modal amplitude coherence is defined as the coherence between the modal amplitude history and the ideal one formed from the initial value of the history and the identified eigenvalue. The MAC is similar to a dot product between the measured vector, called  $\hat{q}_i$ , for each mode  $i$  and the corresponding model response history  $\bar{q}_i$ . The MAC is defined by

$$MAC_i = \frac{|q_i \hat{q}_i^*|}{|q_i \hat{q}_i^*| |\hat{q}_i \bar{q}_i^*|^{1/2}} \quad (3.35)$$

where  $*$  is the complex conjugate transpose. A value near unity indicates the model reproduces the pulse response data [9].

## Chapter 4

# Technique for Modal Analysis in Image Plane

In this chapter the IPMA method is explained. The IPMA method is used when making measurements with the photogrammetric method. The IPMA method differentiates between system and noise modes in the image plane coordinate system and removes the noise from the data. The filtered data prevents some errors in the measurements from propagating through the calculations and diluting the identification results.

### 4.1 Image Plane Modal Analysis

In the traditional photogrammetric method, the locations of points are measured on an image [1]. Photogrammetry is based on the principle that a point, its image, and the focal point of the camera all lie in a straight line. When more than one camera is used, the location of the point in a global coordinate system can be determined from image plane measurements. The least squares method determines the best estimate for the intersection of the lines from each camera for the same point. If there are errors or noise present in one or more of the measurements these errors propagate into the results in the least squares method. The presence of these errors leads to increased uncertainty in the system identification results when using photogrammetric data.

One source of errors in particular is the vibrations specific to the cameras. A small displacement or slight change in the orientation of the camera can result in a large error in the measurement of the point location on the image plane. If the cameras are mounted independent of each other, such disturbances are uncorrelated, and appear at different frequencies in each image plane. The IPMA method is designed to account for some of these disturbances and to remove such contributions from the photogrammetric measurements.

The IPMA method performs system identification on the time series of the points in each camera image plane. For example, if three cameras track the same point  $j$  for period of time  $t$ , each camera will produce two position time series,  $x$  and  $y$ . If the sample rate of the cameras is  $\delta t$ , then the time series will have length  $m = t/\delta t$ . These vectors will be of the form

$$\begin{aligned}\bar{x} &= [x_0, x_1, \dots, x_m] \\ \bar{y} &= [y_0, y_1, \dots, y_m]\end{aligned}\tag{4.1}$$

In the case above, there is a total of 6 position time series containing the location of the point in the image planes of the three cameras.

Each pair of time series is analyzed independently using the ERA method described in Chapter 3. In the ERA method a model of order  $n$  is assumed to represent the system. The results from the analysis of the time series from one camera will produce a set of  $n$  frequencies, corresponding dampings, and confidence indicators. Each camera is analyzed in this manner to produce several sets of frequencies and dampings. Modes with low confidence levels are discarded first. The remaining frequencies for each camera are compared to determine which modes are system modes and which are local or noise modes. System modes will generally appear in each camera at nearly the same frequencies. Local modes will appear at different frequencies for each camera.

The previous step indicates at or near what frequencies system modes are located. To assure coherence between the several sets of data for triangulation purposes, all of the image plane vectors are combined into one matrix and analyzed simultaneously.

While there should be little variation in modal parameters from one image plane to another, this step insures that the frequencies that best represent the modes in all images are obtained. In the case examined here a matrix with 6 columns, each column containing one of the image plane position time series, is analyzed using ERA. The analysis provides coherent frequency and damping values for reconstructing the image plane data.

This yields a set of  $m$  frequencies and  $m$  damping values

$$\begin{aligned}\omega &= [\omega_1, \dots, \omega_m] \quad m \leq n \\ \zeta &= [\zeta_1, \dots, \zeta_m]\end{aligned}\tag{4.2}$$

where  $m$  is the number of system modes identified.

The system modes are used to reconstruct the image plane time series for each camera. The reconstruction uses the model

$$Ax = y\tag{4.3}$$

where  $y$  is the original data matrix and a row of  $A$  is given by

$$A = \left[ e^{-\zeta_1 \omega_1 t} \sin \omega_1 t \quad e^{-\zeta_1 \omega_1 t} \cos \omega_1 t \quad \dots \quad e^{-\zeta_m \omega_m t} \sin \omega_m t \quad e^{-\zeta_m \omega_m t} \cos \omega_m t \right]\tag{4.4}$$

where  $A$  is  $1 \times 2m$ .

The reconstructed data is calculated from the equation

$$x = (A^T A)^{-1} A^T y\tag{4.5}$$

The reconstructed data is used in the triangulation process to find the location of the point in global space. The errors due to local vibrations specific to one camera in the new location are reduced.

## 4.2 Items of Concern

Several items are important to keep in mind when conducting this analysis. The principle that this method is based on is that structural modes will appear in all

cameras. This is true unless the motion due to certain modes is orthogonal, or nearly orthogonal, to the image plane of the camera. Much like accelerometers are designed to measure acceleration in only one direction, cameras detect motion parallel to the image plane and not orthogonal to it. To avoid this problem it is important to give consideration to the location of the cameras recording the motion. Also, the use of more than the minimum number of cameras can help avoid this problem. If a structural mode is edge on to one camera, with three cameras the other two cameras will detect the mode.

Another item of concern is the distribution of targets on the structure being recorded. It is important to have targets located over as wide a range as possible to avoid having targets located at nodes and not detecting the motion due to certain modes. If the targets are too close or there is not enough of them the targets may not indicate that certain modes exist. Targets should be chosen so that an adequate response of the structure can be measured.

A third item is the level of motion that is detectable with photogrammetry. Several studies have demonstrated that subpixel resolution is achievable, specifically [1] and [13]. The detectable displacement is proportional to the field of view. In the experiment described in Chapter 5, a 0.2 pixel resolution is assumed and the images have fields of view set at roughly 120 inches. Assuming the CCD chip is 500 pixels wide, each pixel represents 0.24 inches. Twenty percent of 0.24 inches is approximately 0.05 inches. If the field of view was doubled (240 inches) the motion would have to be greater than 0.1 inches. The smallest motion detectable is important to consider when trying to detect modes with small amplitudes.

## Chapter 5

# EOS-AM Dynamic Test Article

To evaluate the image plane method procedure presented in Chapter 4, experimental data has been taken using the CSI Phase III Evolutionary Test Bed Model [14]. The description of the EOS-AMI testbed model is given in Section 5.1. The experimental set-up and procedure is presented in Section 5.2.

### 5.1 Description

The Controls-Structures Integration (CSI) area developed the CSI Evolutionary Model (CEM) to assist in the development, implementation, and validation of CSI technology. The objective of the CEM3 testbed development is to simulate the overall on-orbit dynamic behavior of the EOS-AM1 satellite. Included in this objective is simulating the low frequency solar array and high gain antenna appendage dynamic interaction [14].

The CEM3 testbed consists of a spacecraft bus structure, two flexible appendages, gimballed instrument simulators, and dummy masses to simulate both science instruments and spacecraft subsystems. The key design criteria for the primary structure design were (1) matching the spacecraft geometry, (2) sufficient torsional stiffness to place the first structural mode above 23 Hz, and (3) supporting the attached payloads and equipment at the proper locations in order to match the overall spacecraft inertia properties. The design of the solar array and high gain antenna of the structure was

driven by the need to meet the associated frequency and stiffness requirements.

Guidelines for the construction of the model included approximating the overall size, shape, and dynamics of the spacecraft while using current suspension system hardware which is capable of supporting up to 2,000 lbs [14]. To simulate the free-free on-orbit boundary conditions, advanced suspension systems are used to support the testbed [14]. The suspension systems provide vertical isolation while long cables provide horizontal isolation. The suspension system results in six low frequency rigid-body suspension modes. The suspension system is designed to minimize the interaction between the 6 suspension modes and the testbed flexible body modes in order to correctly simulate free-free dynamics and the proper coupling between the bus and appendages. To monitor the structure and its vibrational responses, accelerometers are located on the bus and along the solar array appendage. The accelerometers are oriented along the three orthogonal axis of the structure and they are also oriented so as to detect bending about two of the axis.

Suspension stiffness, location of cable attachment points relative to the testbed center of mass, and cable length are the parameters used to drive the rigid body modes below 0.20 Hz. This allows the correct simulation of free-free dynamics and the proper coupling between the bus and appendages. The suspension devices have vertical strokes of +/- 3 inches and an adjustable active stiffness setting ranging from 0.1 lb/in. to 2.0 lb/in. There are 4 devices supporting the bus and one device is used to off-load the mast tip weight. The location of the five suspension cables can be seen in Figs. 5.1 and 5.2.

The main goal of the experiment is to identify the modes of the solar array appendage. The solar array on the CEM3 model is 15 feet in length, roughly one-half the length of the solar array on the EOS-AM1 satellite. In order for the testbed to match the mode frequencies of the satellite's solar array a forty pound weight is attached to the tip of the mast. This results in the first two bending modes of the solar array having frequencies of 0.716 and 0.815 Hz, respectively. These modes are shown in Figures 5.1 and 5.2. These figures show 4 views of the test article (starting in the upper left and going clockwise): 1) side view, 2) oblique view, 3) front view,

and 4) top view. The first view in Figure 5.1 shows the high gain antenna rising from the bus between the suspension cables. In the second view the five cables of the suspension system are shown along with the solar array appendage. The top view of the structure clearly shows the bending mode of the array. In Figure 5.2 the second bending mode and coupling between the appendages is visible in the front view (lower right view).

## 5.2 Experiment Description

The purpose of the IPMA experiment is to evaluate the IPMA method and how it improves the motion measurements using photogrammetry by removing errors due to noise present in the cameras. In order to accomplish this identification the motion of both the root and the tip of the solar array are recorded. Therefore two cameras are focused on both the tip and the root, for a total of four cameras. The views for each camera are shown in Figure 5.3.

The IPMA experiment targeted the first bending mode of the solar array by applying an input to transfer most of its energy into the first mode. The input is a .5 Hz sine wave from a shaker located at one corner of the bus. The .5 Hz is very close to the .65 Hz frequency of the first bending mode. Also, the input was applied in the yaw (along the Y-axis) direction, which is the primary direction of the first bending mode.

The four cameras used are CCD cameras that were previously installed in the laboratory to observe the test structure during experiments. Therefore the locations of these cameras were predetermined and could not be changed. All cameras are identical and the zoom capability is from 16 mm to 160 mm. The cameras record at the rate of 30 frames per second (30 Hz). For this experiment the field of view for each camera was set to approximately 10 feet in order to simulate the field of views for PASDE.

The video data was recorded on four identical S-VHS video recorders. To synchronize the video data, two strobe lights were placed so that at least one light appeared

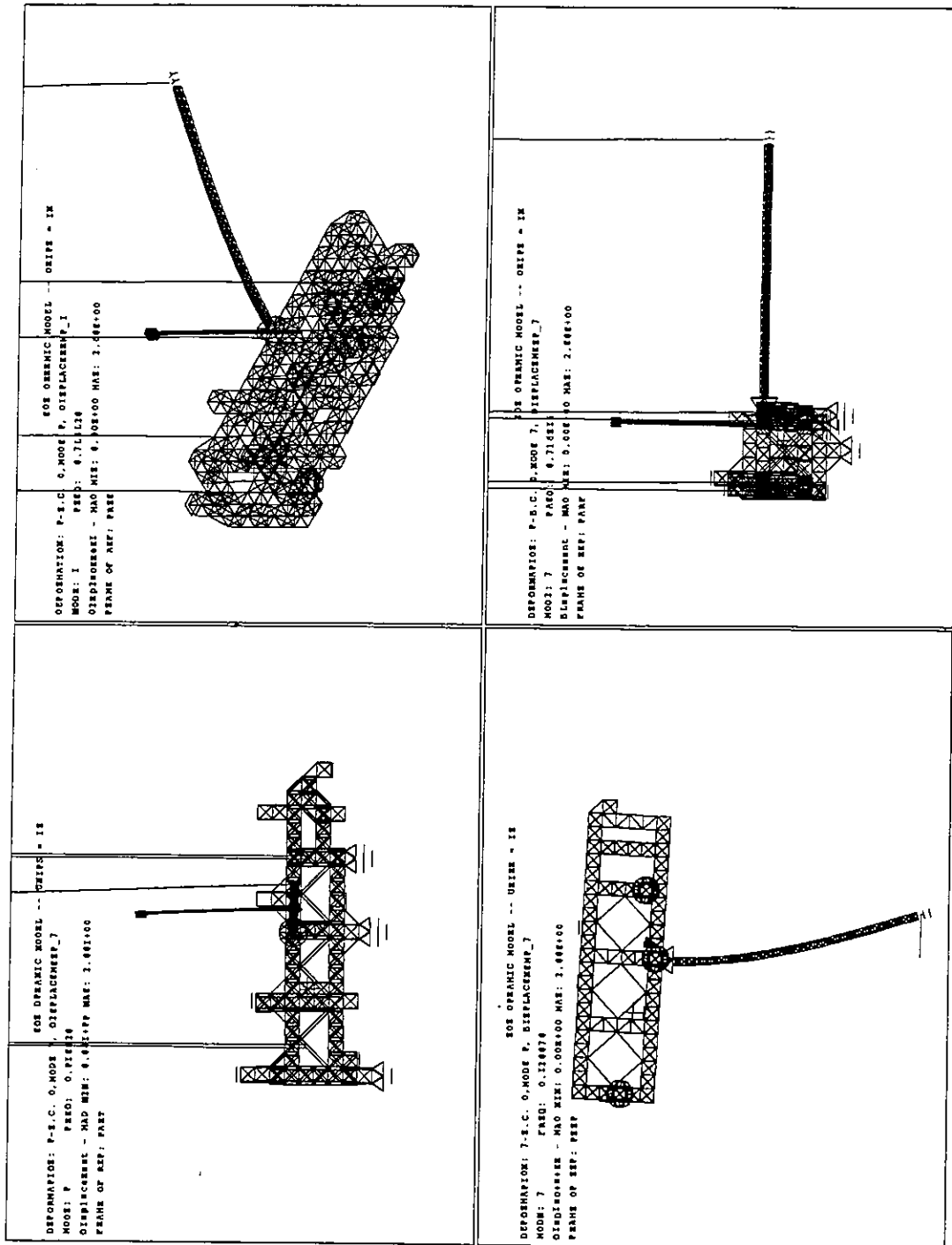


Figure 5.1: First Bending Mode of Solar Array Appendage

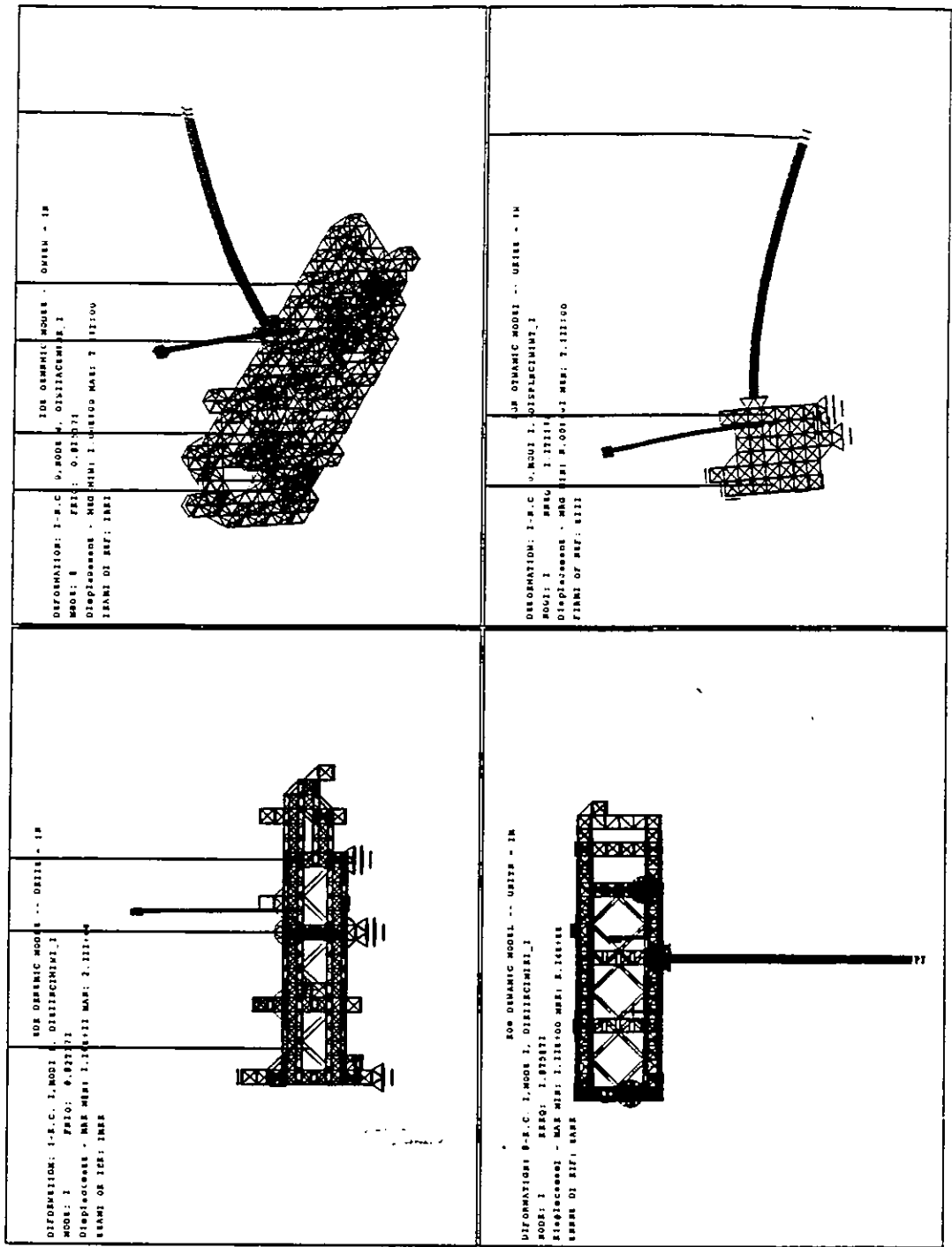
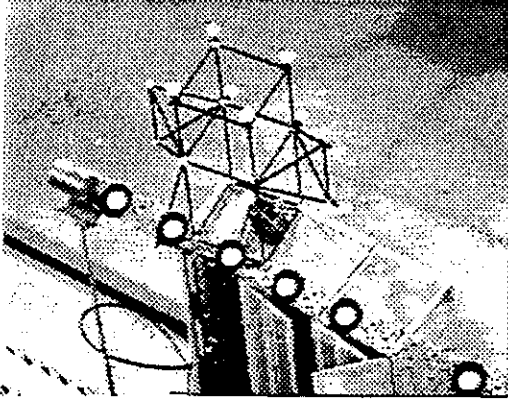
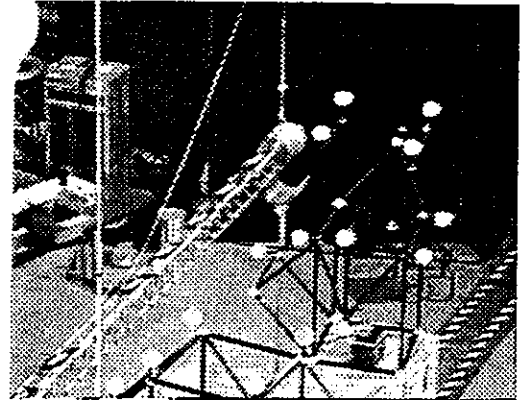


Figure 5.2: Second Bending Mode of Solar Array Appendage

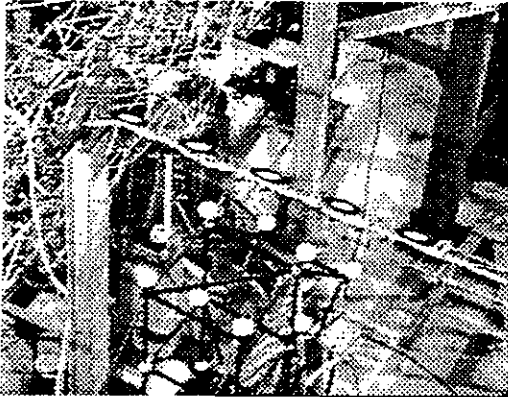
Camera 1



Camera 2



Camera 3



Camera 4

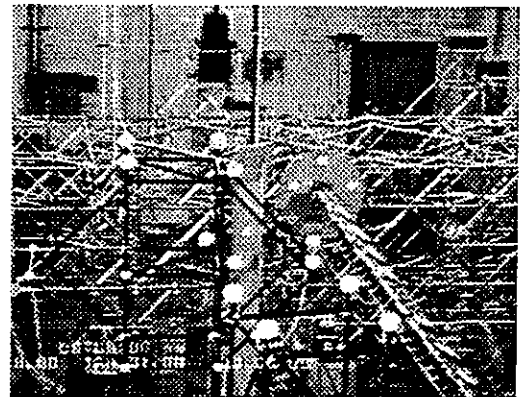


Figure 5.3: Camera Views of EOS-AM1 Testbed

in each camera image. The two lights were sent a signal at the beginning of each free-decay period to synchronize the tapes. The signal was also sent to the digital data acquisition system that was recording the data from the accelerometers located along the solar array appendage, including the base plate and on the mass located at the tip.

The targets placed on the solar array were white circles four inches in diameter on a black concentric circle eight inches in diameter. These targets can be seen clearly in the view from camera 1 in Figure 5.3. Additional two inch diameter targets were placed on the base plate at the root of the solar array. These targets can best be seen slightly to the right of center in the view from camera 4 in Figure 5.3. There were thirteen targets on the structure.

To assist in the bundle adjustment method, free standing control points were placed near the testbed such that a sufficient number of points appeared in each camera (see Figure 5.3). The locations of these control points were determined using independent measurement techniques. Nineteen control points were measured for use with the bundle adjustment method.

The protocol used during the experiment was as follows:

- 1) Each camera was set at a focal length which provided a field of view of 10 feet at the testbed.
- 2) Begin input to the structure using a shaker connected at one corner of the bus. The input is designed to excite the first bending mode of the solar array appendage and provide approximately 2 inches of displacement of the solar array at the tip.
- 3) While the testbed is coming to steady state, the video recorders record the camera images.
- 4) Once the testbed reaches steady state, the input is stopped, and the strobe lights are flashed to mark the beginning of the free decay period.
- 5) The data recording period lasts one minute, in which time the testbed comes to rest.

## Chapter 6

# Image Plane Modal Analysis

## Results

An experiment using the EOS-AM1 dynamics testbed was conducted to demonstrate the effectiveness of the image plane identification method. The first bending mode of the solar array appendage was targeted by the excitation while both accelerometer and video data recorded the response of the structure. The accelerometer data provides a baseline comparison for the photogrammetric data. System identification using the ERA analysis was performed on three sets of data, The accelerometer data, the photogrammetric data, and the IPMA data. The results for all three are compared to show the effectiveness of the image plane data versus standard methods.

### 6.1 Accelerometer Data System Identification Results

Accelerometers are located along the solar array appendage and on the base plate of the appendage. Appendix B contains the 24 time series used in the identification analysis and the location and orientation of each device is listed. Approximately 16 seconds of free-decay data was used in the analysis. This allowed the amplitude to decay to 1/3 original signal strength. The bandwidth of the accelerometer data is 0 to

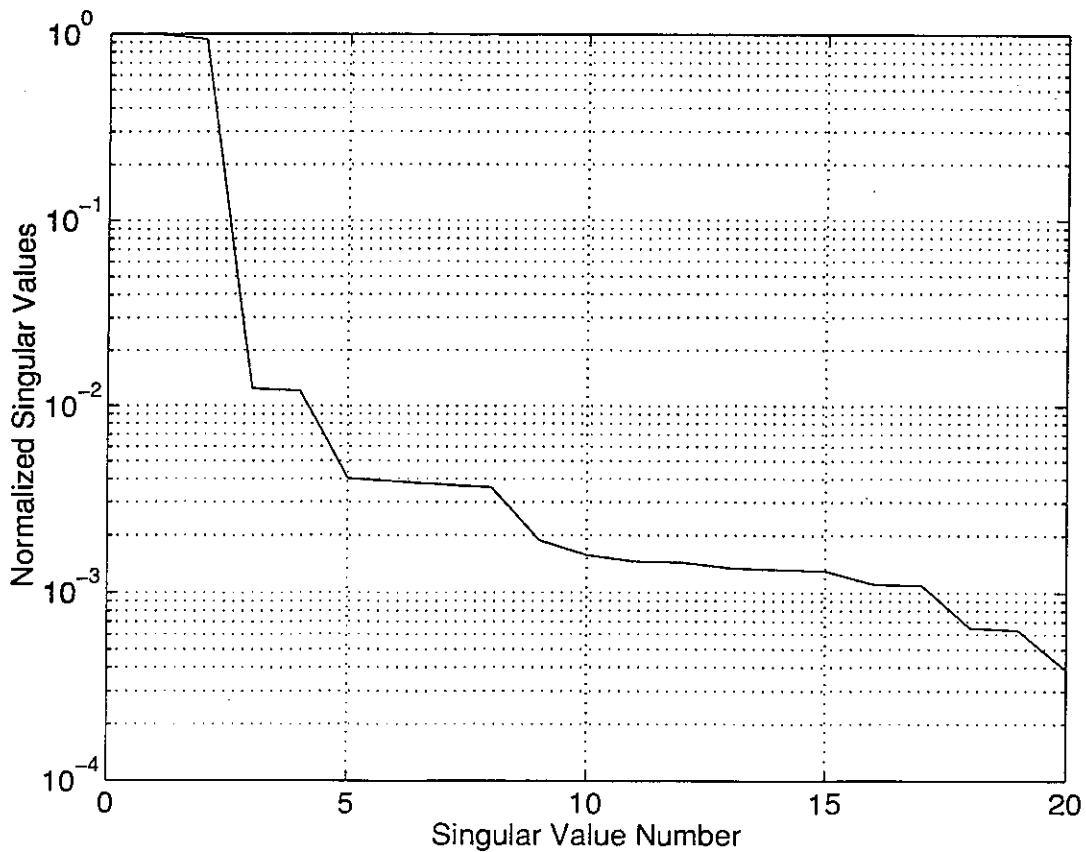


Figure 6.1: Singular Value Decomposition for Accelerometer Data

6 Hz. The next part in the analysis consisted of determining the assumed number of modes for the system. This was done by studying the singular value decomposition of the Hankel matrix. Theoretically, the number of non-zero singular values is the rank of the Hankel matrix. However, due to noise none of the singular values will be zero. Therefore a cut-off value needs to be determined. If the difference between successive singular values is significant then the selection is simple. The first 20 singular values for the accelerometer data are shown in Figure 6.1. There are several drastic changes in the slope shown in the figure. Using  $10^{-2}$  as the cut-off value, 2 strong modes can be expected and leads to a rank of the system of 4. However, it is important to account for the noise and error modes present in the system. To account for the noise, modes are included in the analysis in an attempt to model the noise. In this way the noise modes can be identified and removed from the system. In the analysis, a state model with order of 20 was selected.

The ERA analysis determines a best fit for the data using a least squares method. One input parameter that is varied in this optimization process is the number of block row shifts in the Hankel matrix. The number of row shifts is the number of time-shifted sub-matrices that appear in the Hankel matrix. These sub-matrices are the Markov parameters of the system and are described in Chapter 3, 3.14 and 3.15. Increasing the number of row shifts causes the analysis to target certain frequencies. For this reason, the number of row shifts is incremented from 2 to 40 in the analysis.

The identified natural frequencies as a function of the number of block row shifts are plotted in Figure 6.2. Each row of results corresponds to a separate ERA analysis with the specified number of row shifts. Each detected mode is represented by a vertical dash at the associated frequency. The confidence level in each result is expressed by the length of the vertical dash, which is proportional to the MAC value. If the highest value is attained, then the MAC value is 1 and the distance between minor tick marks on the vertical axis is filled [15]. An example of the output from the ERA analysis is shown in Table 6.1. Only roots with normalized MAC values above .0005 were plotted.

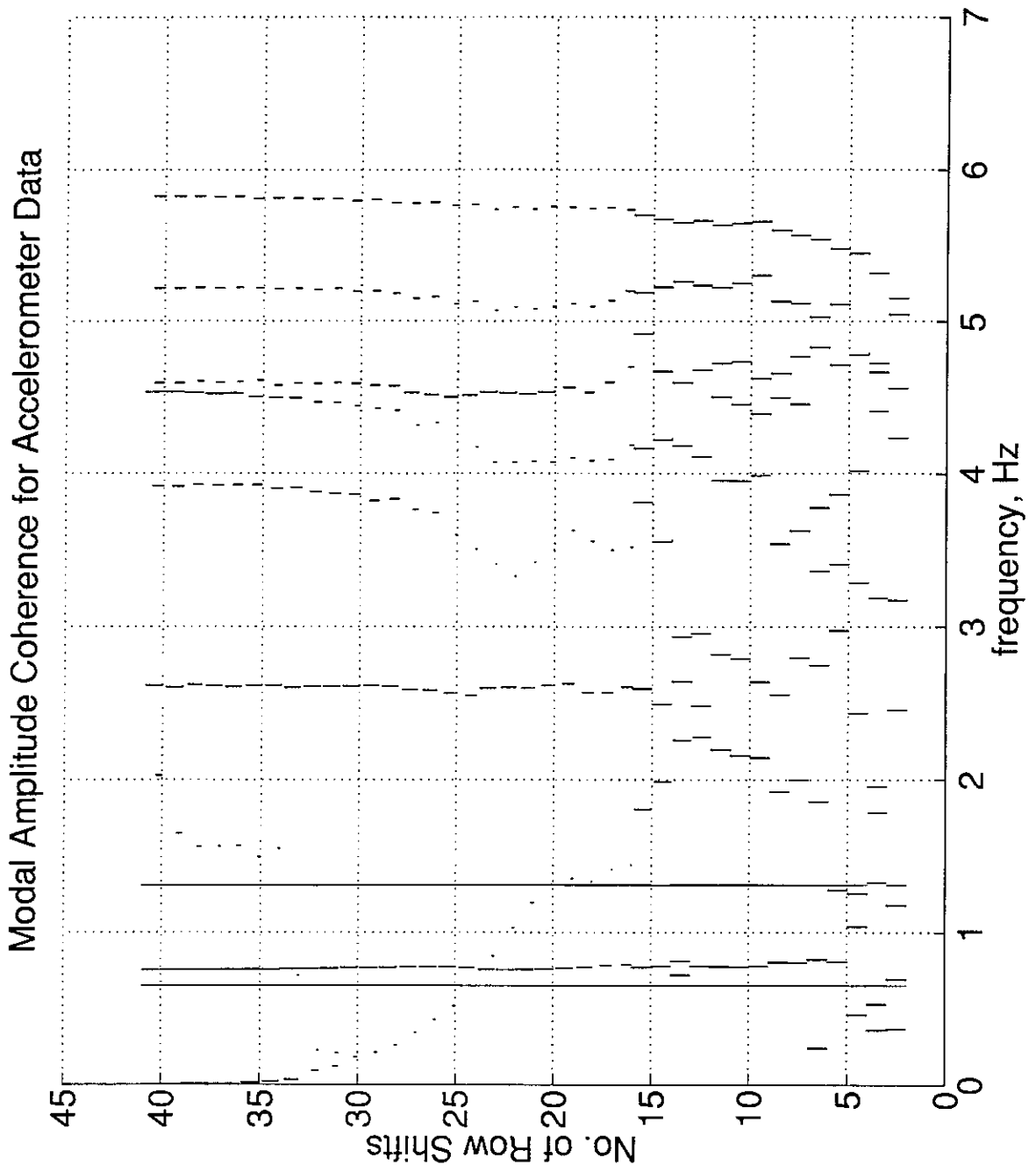


Figure 6.2: Modal Amplitude Coherence for Accelerometers vs. No. of Row Shifts

Three modes at frequencies 0.648 Hz, 0.758 Hz, and 1.31 Hz appear strong over the entire range of row shifts. The first mode at 0.648 Hz is the first bending mode of the solar array primarily in the X-direction. The mode at 0.75 Hz is the first bending mode primarily in the z-direction. The last mode at 1.31 Hz is a coupling mode between the high gain antenna and the solar array appendage.

While the analysis identified these modes even with few row shifts, the other modes are not as well identified. In fact, with 2 to 15 row shifts, frequencies identified vary widely from one analysis to the next even though the confidence level is quite high for each mode. For row shifts between 15-25, the analysis began to target certain frequencies, but the confidence levels are small. For row shifts above 25 the confidence levels for each mode identified increased to constant values for a large number of row shifts.

A possible explanation for these results is as follows. The MAC values are calculated by comparing predicted modal amplitude histories with the corresponding real histories. With a minimum number of row shifts it is more likely to have a good comparison between the two histories. As the number of row shifts increases the more dominant frequencies are repeated throughout the Hankel matrix. This also explains why the confidence level increases for some frequencies as the number of row shifts increases. However, even though the MAC values increase for the other modes, they are still small enough to be regarded as noise modes present in the system.

Another indicator that is used in judging the validity of modes is the corresponding damping value. Figure 6.3 shows an expanded view of the frequencies between 0.6 and 0.7 Hz. Along with the frequency, the damping and MAC values are shown as the number of row shifts is varied. The plots show very little variation in any of the values indicating a high degree of confidence for the mode over the entire range of row shifts.

Figure 6.4 shows an expanded view of the frequency range from 2.4 Hz to 3.0 Hz. For this mode, the damping and MAC values vary as compared with the values in Figure 6.3. The MAC values are all below 0.9 indicating it is not a good candidate for a structural mode. Changes in the damping values vary from one run to the next

Table 6.1: ERA Results For Accelerometers with 20 Block Row Shifts

Root No.	Frequency	Damping ,%	SVD	MAC
1	1.3170	30.519	1.0586e-03	0.12374
2	1.3170	30.519	1.0586e-03	0.12374
3	3.5029	3.3530	9.8402e-04	0.063750
4	3.5029	3.3530	9.8402e-04	0.063750
5	4.0766	2.7601	9.4847e-03	0.23090
6	4.0766	2.7601	9.4847e-03	0.23090
7	5.0941	2.0343	1.5381e-02	0.17458
8	5.0941	2.0343	1.5381e-02	0.17458
9	5.7582	1.5925	1.9132e-02	0.28747
10	5.7582	1.5925	1.9132e-02	0.28747
11	2.6156	2.1067	7.3378e-03	0.64930
12	2.6156	2.1067	7.3378e-03	0.64930
13	4.5398	0.41885	3.8382e-03	0.88087
14	4.5398	0.41885	3.8382e-03	0.88087
15	0.64815	1.2871	1.0000e+00	0.99885
16	0.64815	1.2871	1.0000e+00	0.99885
17	1.3104	0.56441	1.0493e-01	0.99041
18	1.3104	0.56441	1.0493e-01	0.99041
19	0.75828	0.40942	3.8014e-02	0.93331
20	0.75828	0.40942	3.8014e-02	0.93331

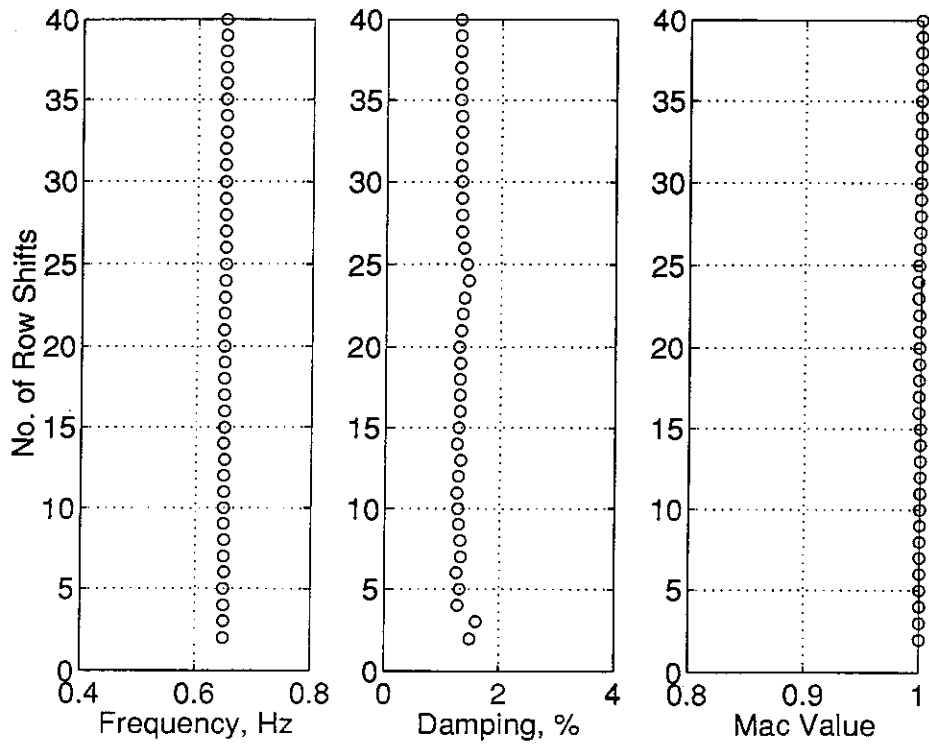


Figure 6.3: Identification Results at 0.65 Hz, Accelerometer Data

also indicate that this is not a good candidate mode. Figure 6.5 shows the mode in the 5 Hz to 6 Hz range. The damping and MAC values show that this mode is a weakly excited structural mode because of the variation in the damping value and the low MAC value.

The conclusion that is drawn from these results is that three structural modes, at 0.65 Hz, 0.76 Hz, and 1.31 Hz are strongly excited in this experiment. These modes should be included when modeling the structure.

Figures 6.6 and 6.7 show comparisons between measured free-decay data and reconstructed free-decay data from the ERA output using only the three strongest modes, 0.65 Hz, 0.76 Hz, and 1.31 Hz. Both figures show good agreement. In Figure 6.7, some difference can be seen due to higher frequencies present in the data. This is to be expected since only low frequency modes were used to reconstruct the data.

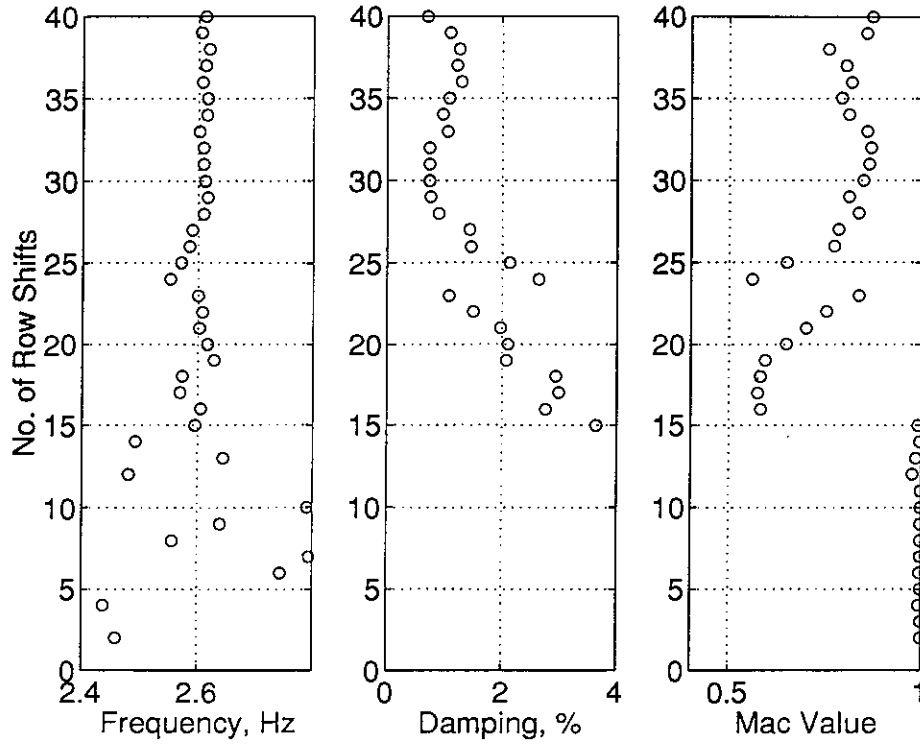


Figure 6.4: Identification Results at 2.6 Hz, Accelerometer Data

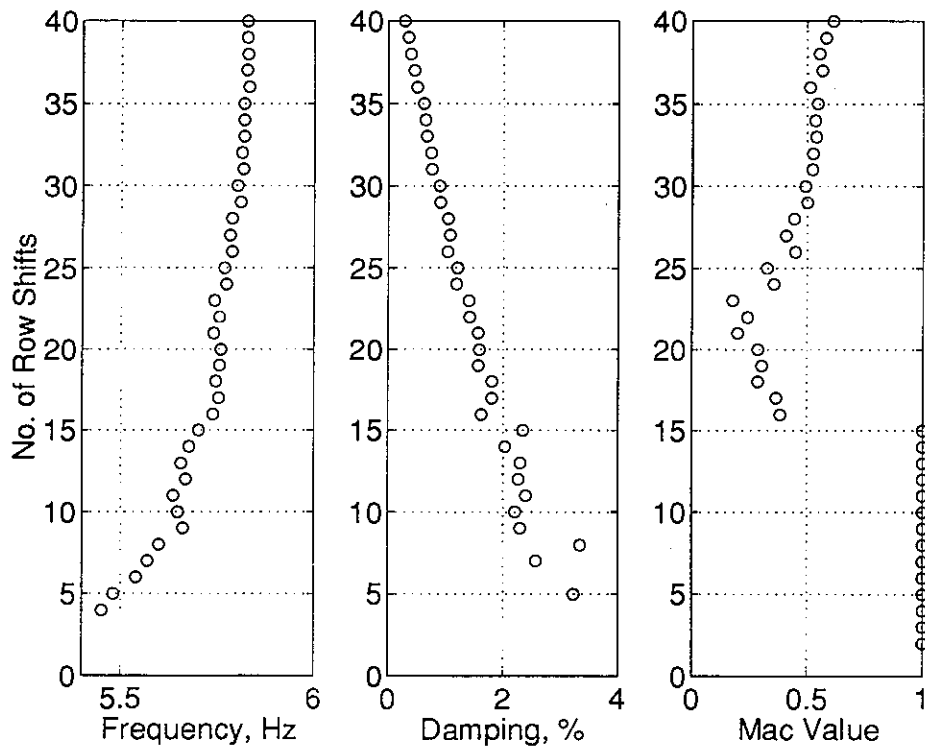


Figure 6.5: Identification Results at 5.8 Hz, Accelerometer Data

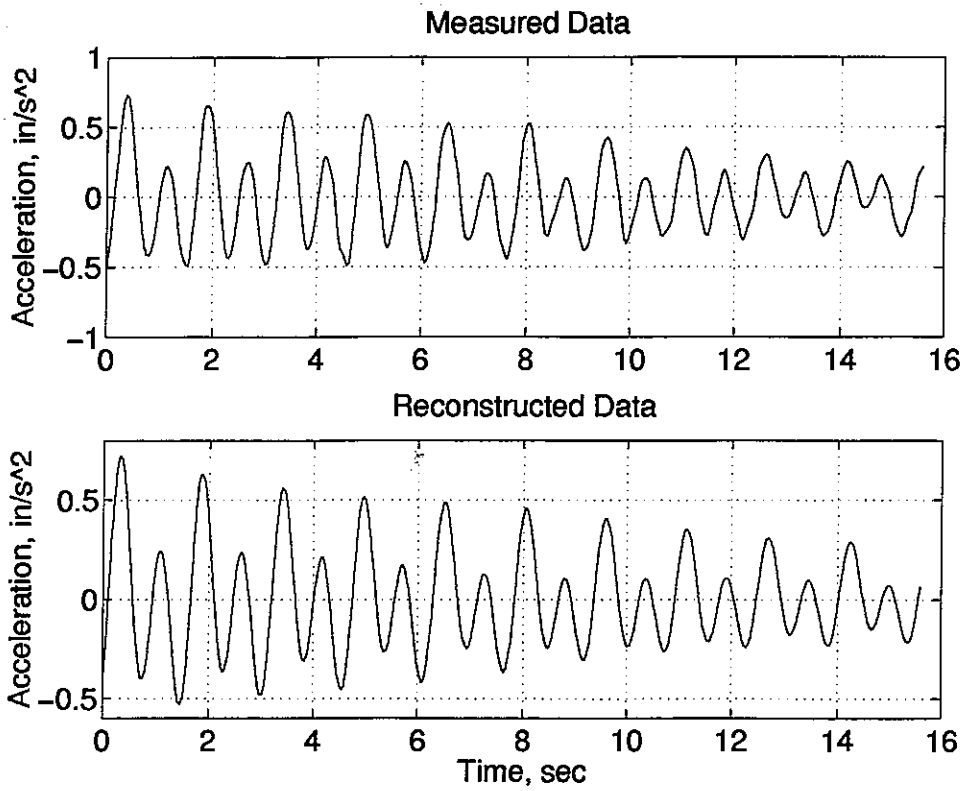


Figure 6.6: Comparison of Measured and Reconstructed Free-Decay Data, Accl.# 1

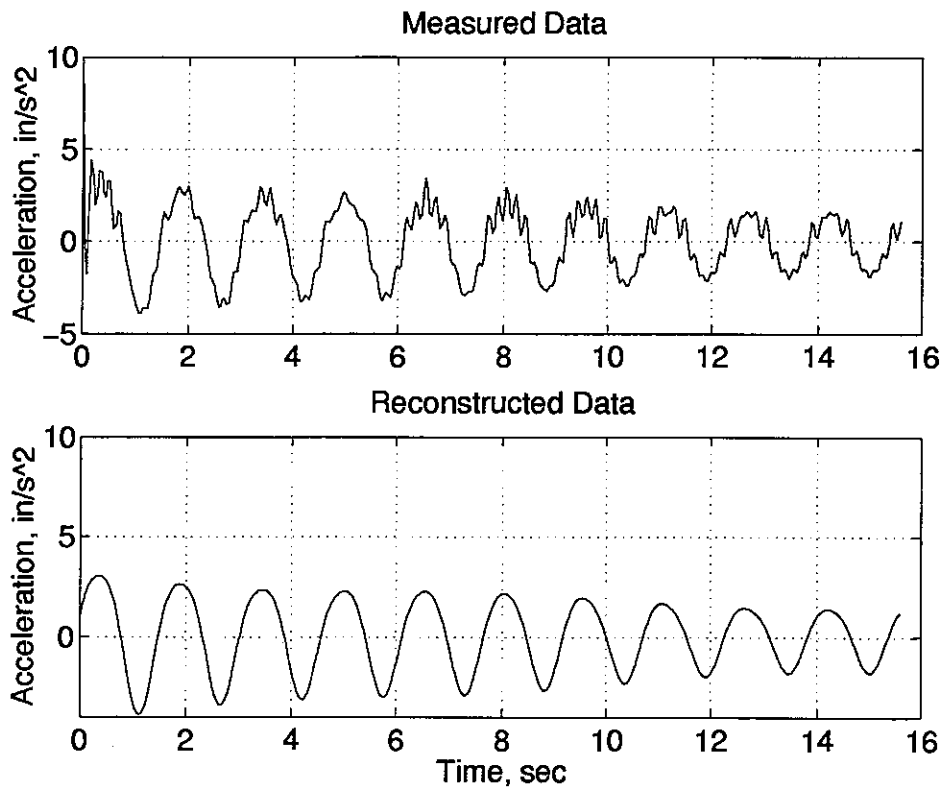


Figure 6.7: Comparison of Measured and Reconstructed Free-Decay Data, Accl# 11

## 6.2 Photogrammetric Analysis Results

The system modal frequencies were identified in the previous section. The three system modes (0.65 Hz, 0.76 Hz, and 1.31 Hz) are the dominant modes. The photogrammetric data is analyzed in this section. The results from the photogrammetric analysis is compared to the accelerometer analysis in this section.

The video data was digitized at 10 Hz for each of the four cameras. Both the calibration targets and the motion targets on the structure were tracked for each camera providing the time series for each point. The locations of a number of calibration points were known, so the photo resection method described in Section 2.2.3 was used to determine the camera parameters for the experiment. Once completed, the triangulation of the motion targets from image space to object space was performed. The time series of the targets are presented in Appendix C.

Figure 6.8 shows the same type of plot as Figure 6.1 but uses the triangulated data in this case. The singular value decomposition indicates that only one strong mode is present in the triangulated data along with two secondary modes. From Figure 6.9 the strongest mode is identified at 0.65 Hz. The two secondary modes are located at 1.29 Hz and 0.13 Hz. The modes at 0.65 Hz and 1.29 Hz are to be expected but the mode at 0.133 Hz is not. This mode is explained by noting that the test article has 6 rigid body suspension modes, and all of them have frequencies below 0.2 Hz. This mode represents a pendulum-like mode due to the suspension system.

Another important fact to take from Figure 6.9 is that the ERA analysis does not identify the second bending mode located at 0.75 Hz. In the range of 25 to 35 row shifts the analysis identifies a mode near the frequency but the confidence level is very low. This indicates the motion due to this mode is not as strong as the motion from the other modes. A reason for this is this mode is not excited as much as the first bending mode.

Figure 6.10 shows the frequency, damping, and MAC values of the 0.65 Hz bending mode. Much like the previous results, this mode is very strong and both indicators show high confidence levels for the mode. More interesting results can be seen in Fig-

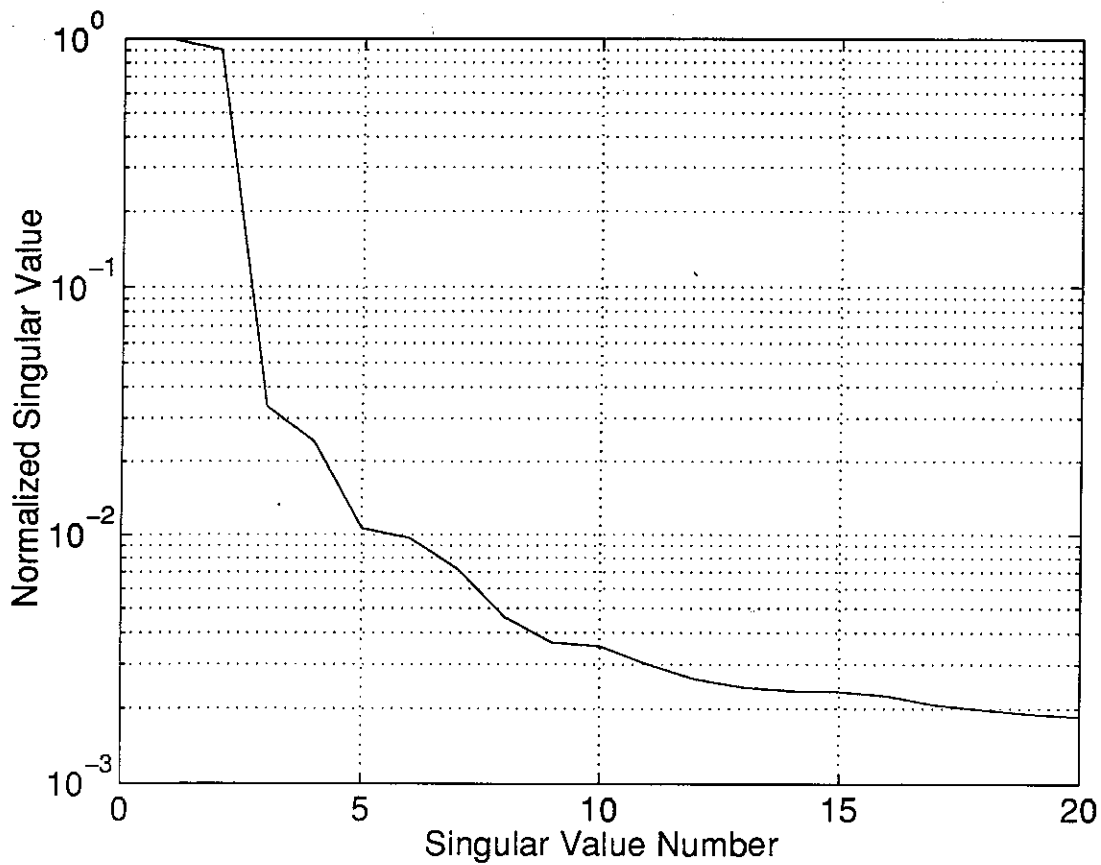


Figure 6.8: Normalized Singular Value Decomposition For Triangulated Data

ures 6.11 and 6.12. The appendage coupling mode in Figure 6.11 demonstrates the necessity to include a large number of row shifts in the Hankel matrix. Not until the Hankel matrix has 35 row shifts does the mode at 1.29 Hz reach acceptable confidence levels. Figure 6.12 shows the MAC values for the 0.13 Hz mode never obtain a value above 0.9, which is the cut-off for accepting or rejecting modes as part of the system. Also, damping values continue to vary even with a large number of row shifts. This demonstrates that this mode should not be included when modeling the system.

Figures 6.13 and 6.14 show video data and reconstructed data. The reconstructed data uses only the two strongest modes, at 0.65 Hz and 1.29 Hz. While there is good agreement between the two sets of data, some differences can be seen, especially later in time. This is a result of analysis failing to identify the second bending mode at 0.75 Hz.

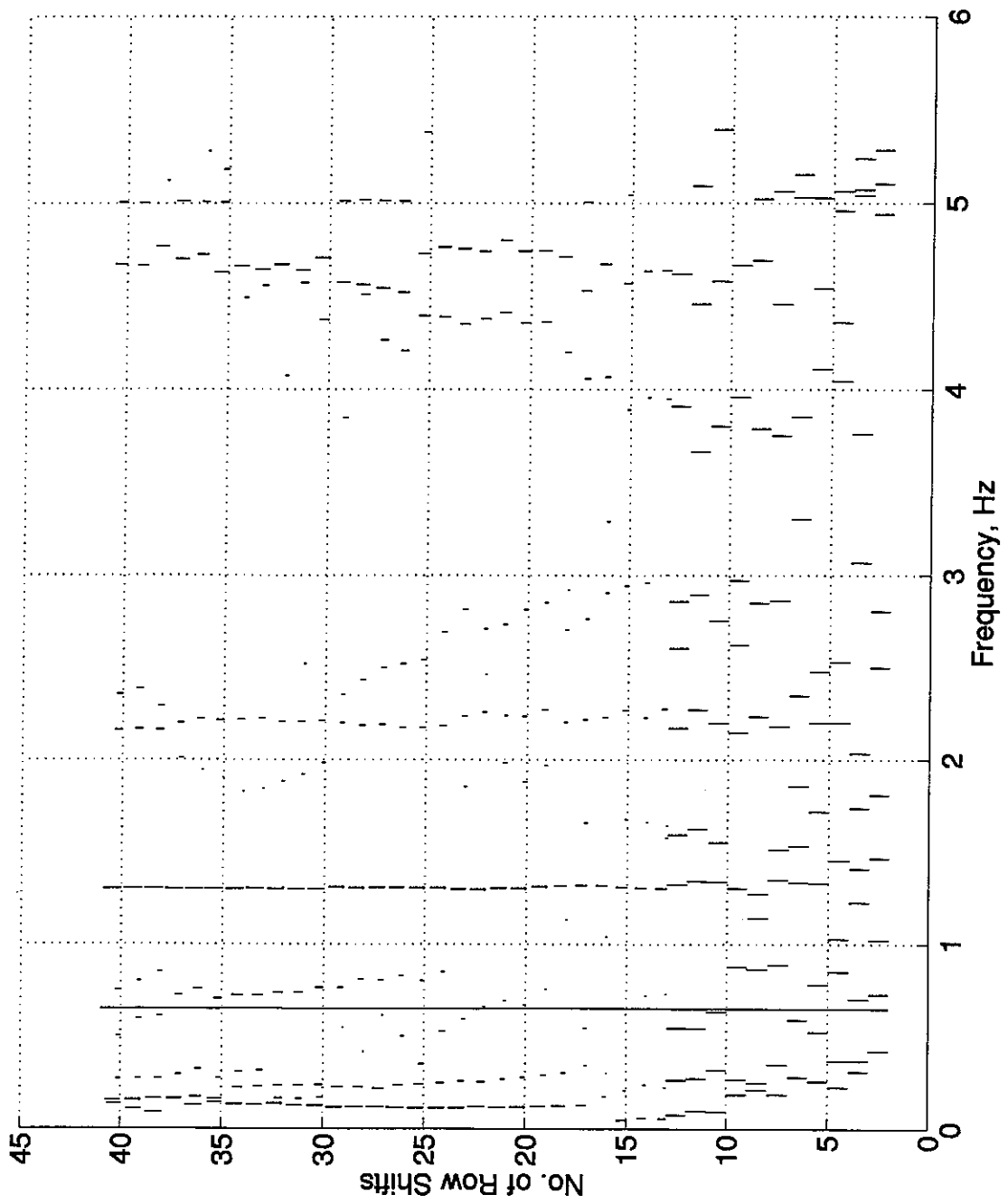


Figure 6.9: Modal Amplitude Coherence For Triangulated Data

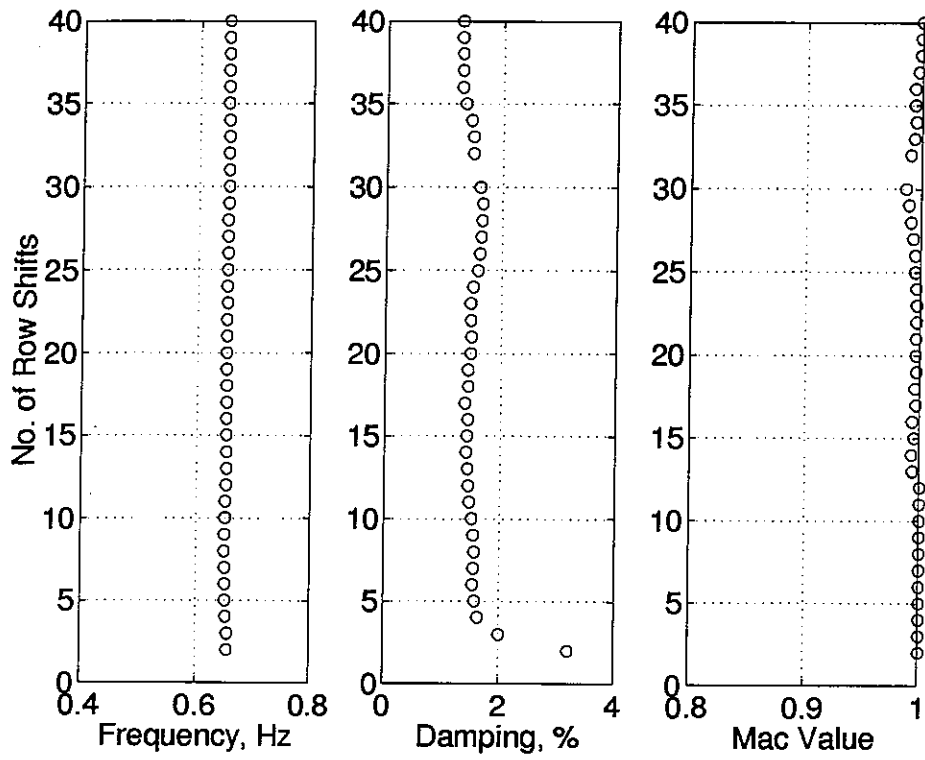


Figure 6.10: Identification Results at 0.65 Hz, Triangulated Data

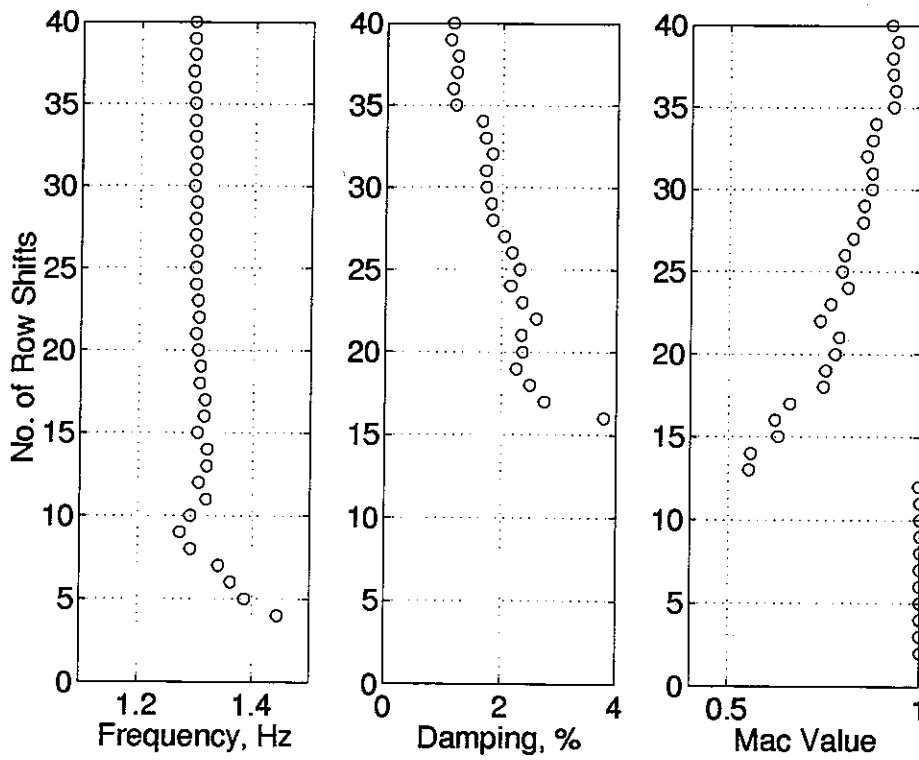


Figure 6.11: Identification Results at 1.29 Hz, Triangulated Data

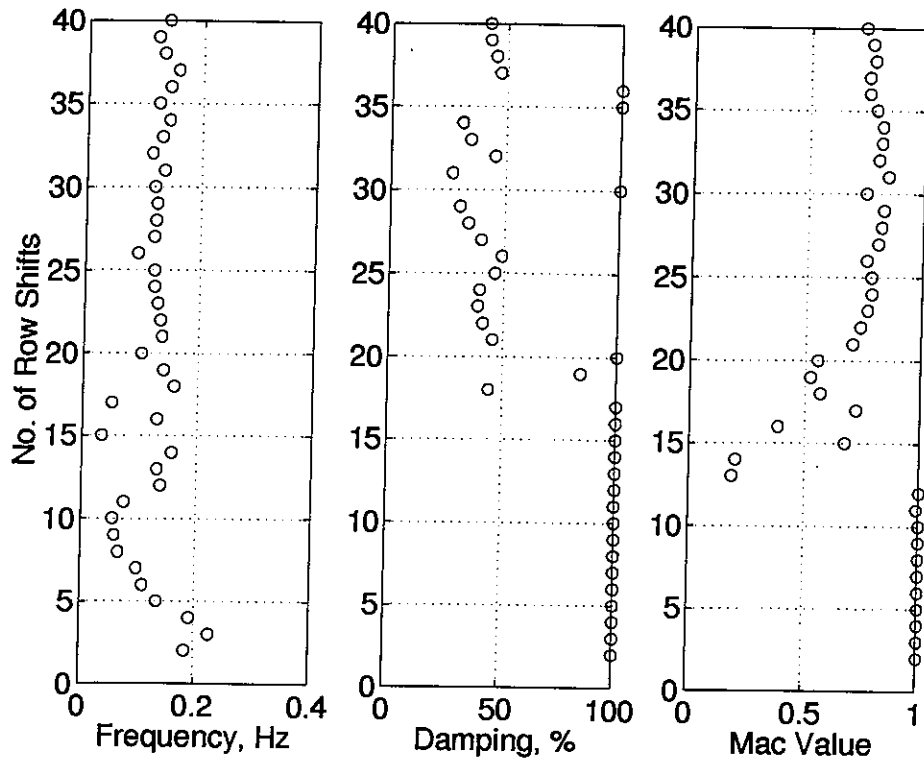


Figure 6.12: Identification Results at 0.12 Hz, Triangulated Data

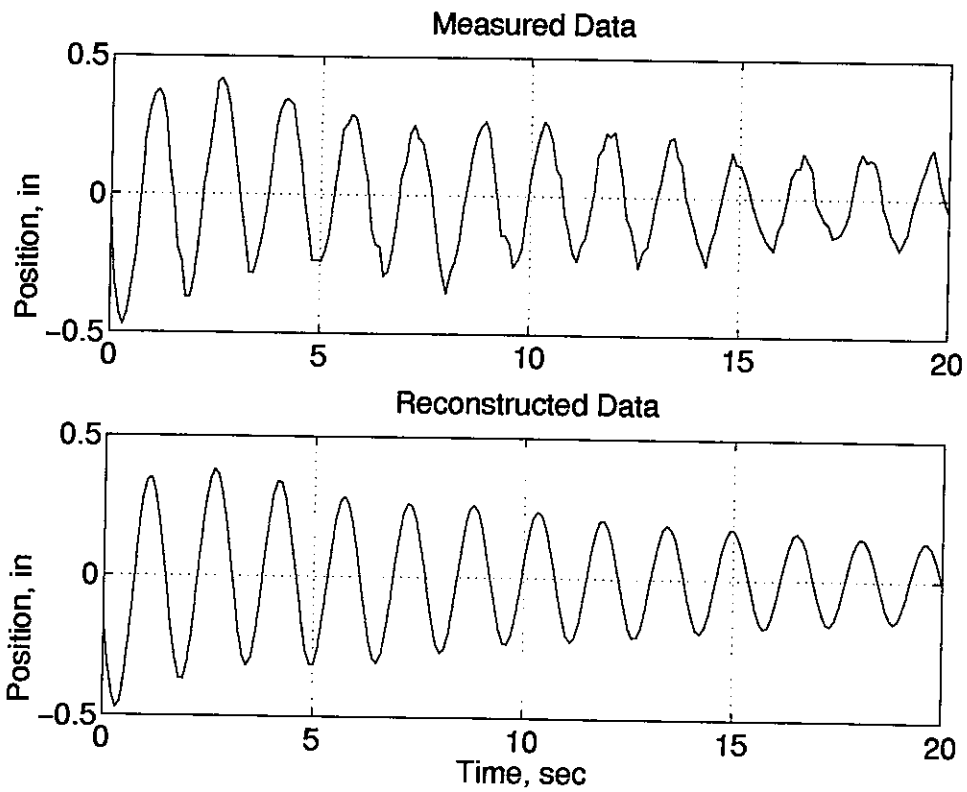


Figure 6.13: Comparison of Actual and Reconstructed Data, Target #1 X Dir.

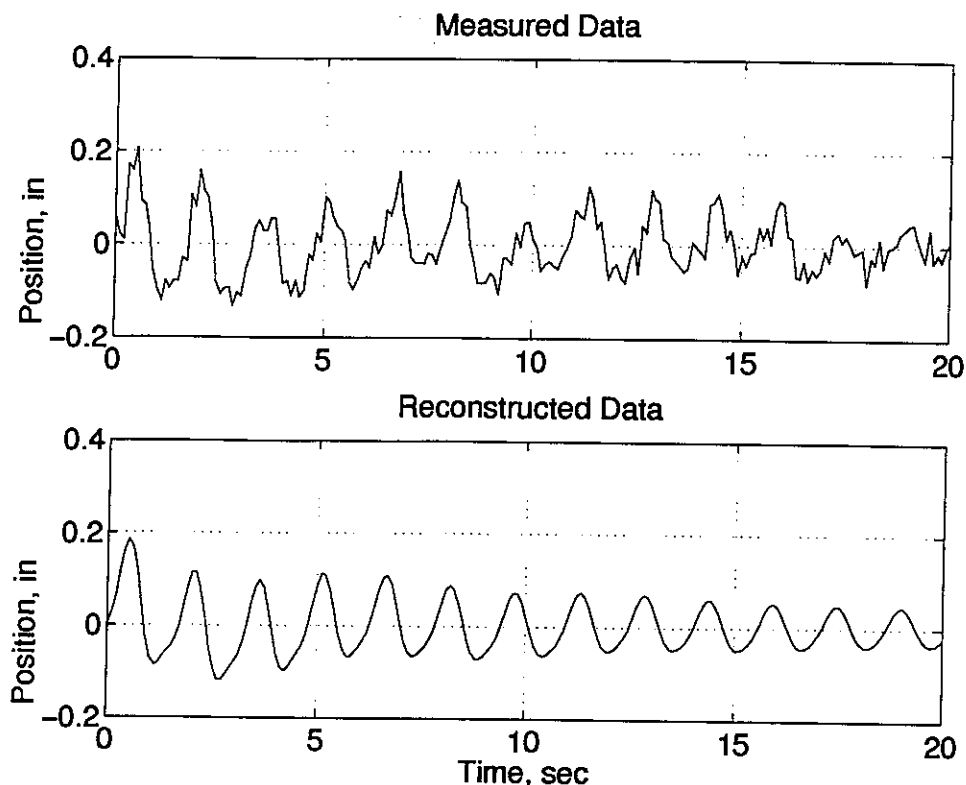


Figure 6.14: Comparison of Actual and Reconstructed Data. Target #1 Y Dir.

### 6.3 Image Plane Analysis Results

The IPMA method identifies modes local to each camera. These local modes are removed from the measurements and reduces some of the noise present in the measurements. The IPMA method consists of several steps:

- 1) The  $x, y$  motion series in each image plane were analyzed separately using the ERA. Comparing the results from the separate analysis identifies which modes were system modes and which ones were local to each camera.
- 2) The  $x, y$  motion series were combined and analyzed using the ERA. This assures coherence between the system frequency and damping values. These values were used to reconstruct the  $x, y$  motion in each image plane.
- 3) The reconstructed motion series were used to triangulate the global motion series of the targets.

- 4) The global series were analyzed using the ERA to provide the mode shapes for the appendage.

The vertical and horizontal histories of the targets in each camera plane are shown in Appendix D. First, each camera is analyzed separately using the ERA program. As defined in Chapter 5, cameras 1 and 2 are focused on the tip of the appendage and cameras 3 and 4 are focused on the root of the appendage. The results for camera 1 are shown in Figure 6.15. The 0.65 Hz bending mode is the strongest mode, and the 0.12 Hz rigid body suspension mode is also predominant. It is interesting to note three other observations. One, the bending mode at 0.75 Hz is stronger in this camera plane. Recall that in the triangulated data this mode did not appear with a high confidence level. Second, all of the modes in this image are below 2 Hz. Third, the coupling mode at 1.30 Hz is not detected by this camera.

One reason for several modes not being detected by the camera is the orientation of the camera with respect to the motion induced by a certain mode. The camera can not detect motion that is orthogonal to the image plane. The coupled mode, and to a lesser extent, the 0.75 Hz bending mode are orthogonal to the image plane of camera 1. This is why more than the minimum number of cameras should be used in any system identification process. This will help ensure that all modes will appear in at least two cameras and make certain they are not dismissed as noise or local modes.

Figure 6.16 presents the ERA analysis for camera plane 2. In this plot all 3 system modes are present and all 3 have high confidence levels.

An analysis of camera 3 is shown in Figure 6.17. The two predominant modes are at 0.65 Hz and 0.12 Hz. What is interesting is the complete lack of indication of the other bending and coupled modes. Examining Figure 6.18 and the image plane 4 analysis, a similar situation is shown. The reason neither of these analyses detected these modes is that the structure was driven to excite the first bending mode. Therefore the motion of the root is due to the free-decay of this mode and neither of the other two modes are present.

Figures 6.17 and 6.18 demonstrate the usefulness of looking at each image plane separately. Both cameras show modes between 2 Hz and 5 Hz. At various number

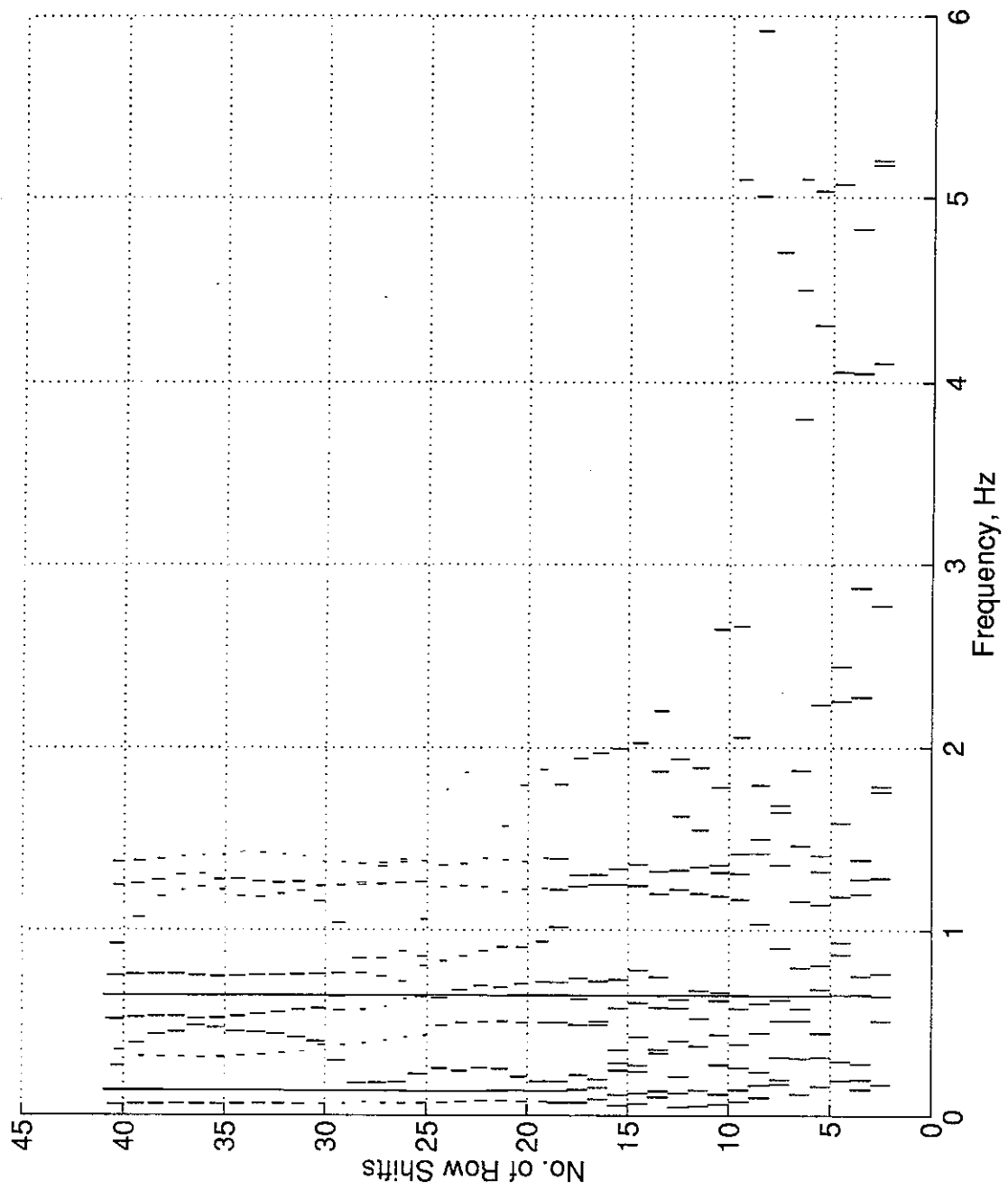


Figure 6.15: Modal Amplitude Coherence for Image Plane 1

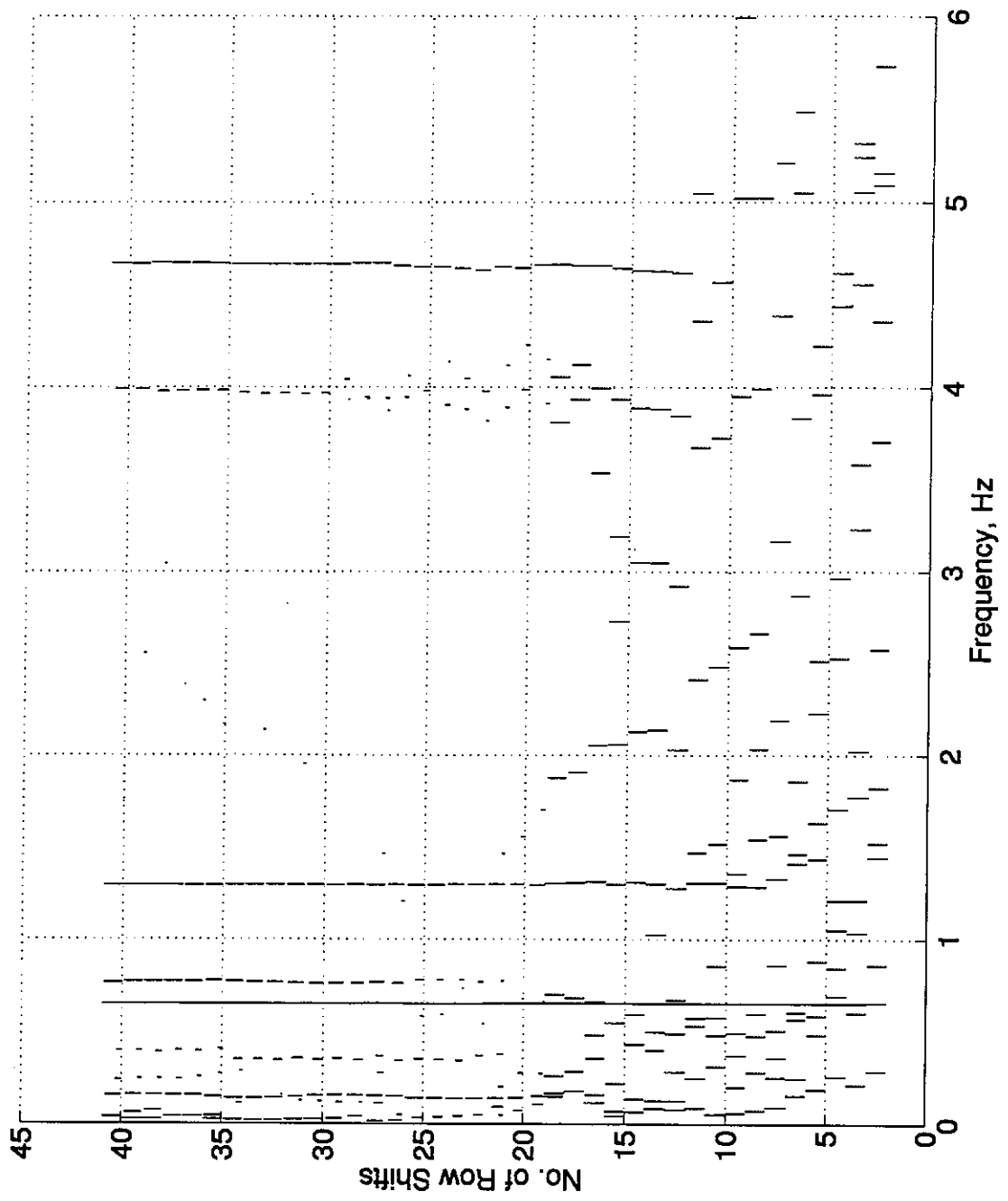


Figure 6.16: Modal Amplitude Coherence for Image Plane 2

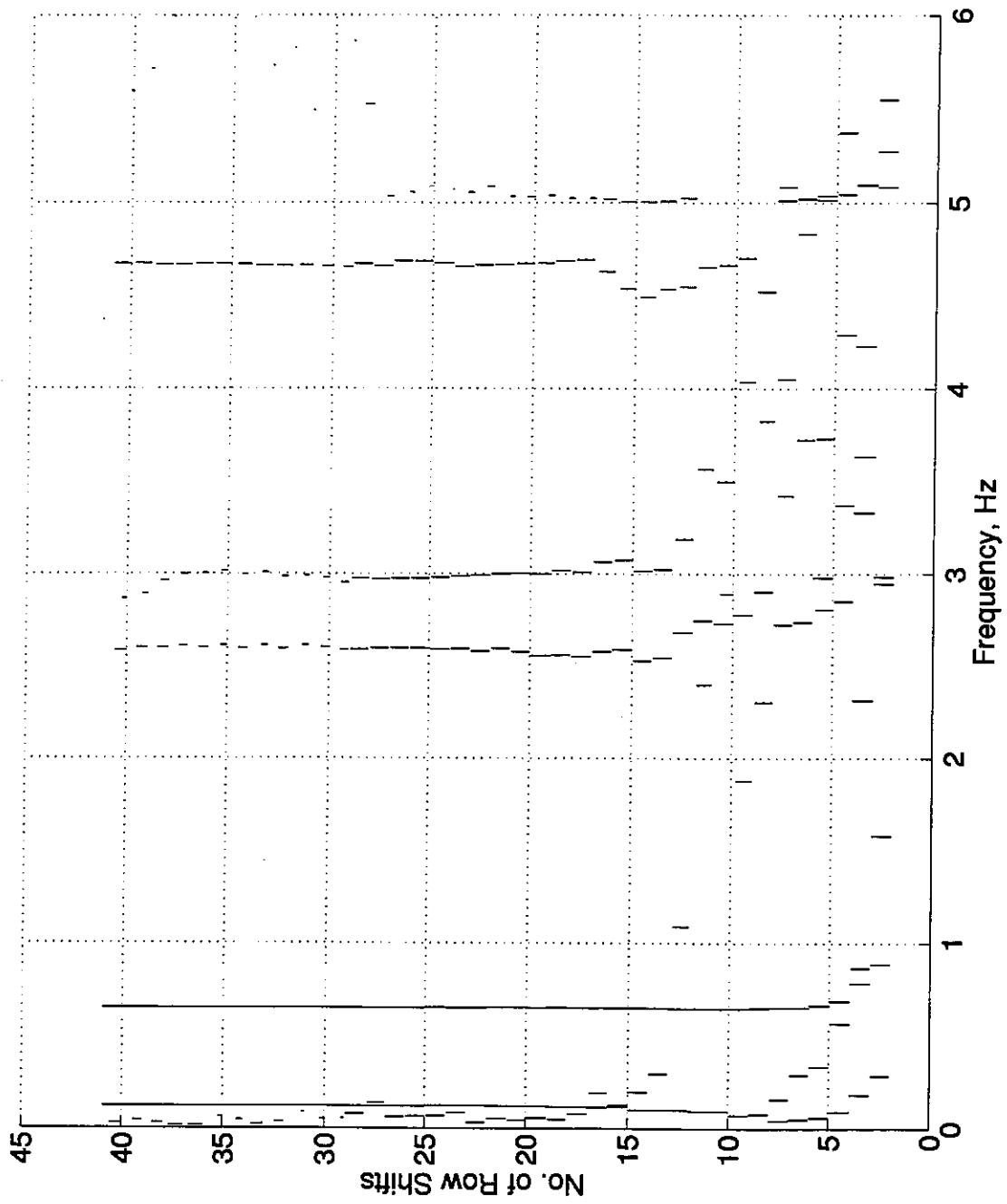


Figure 6.17: Modal Amplitude Coherence for Image Plane 3

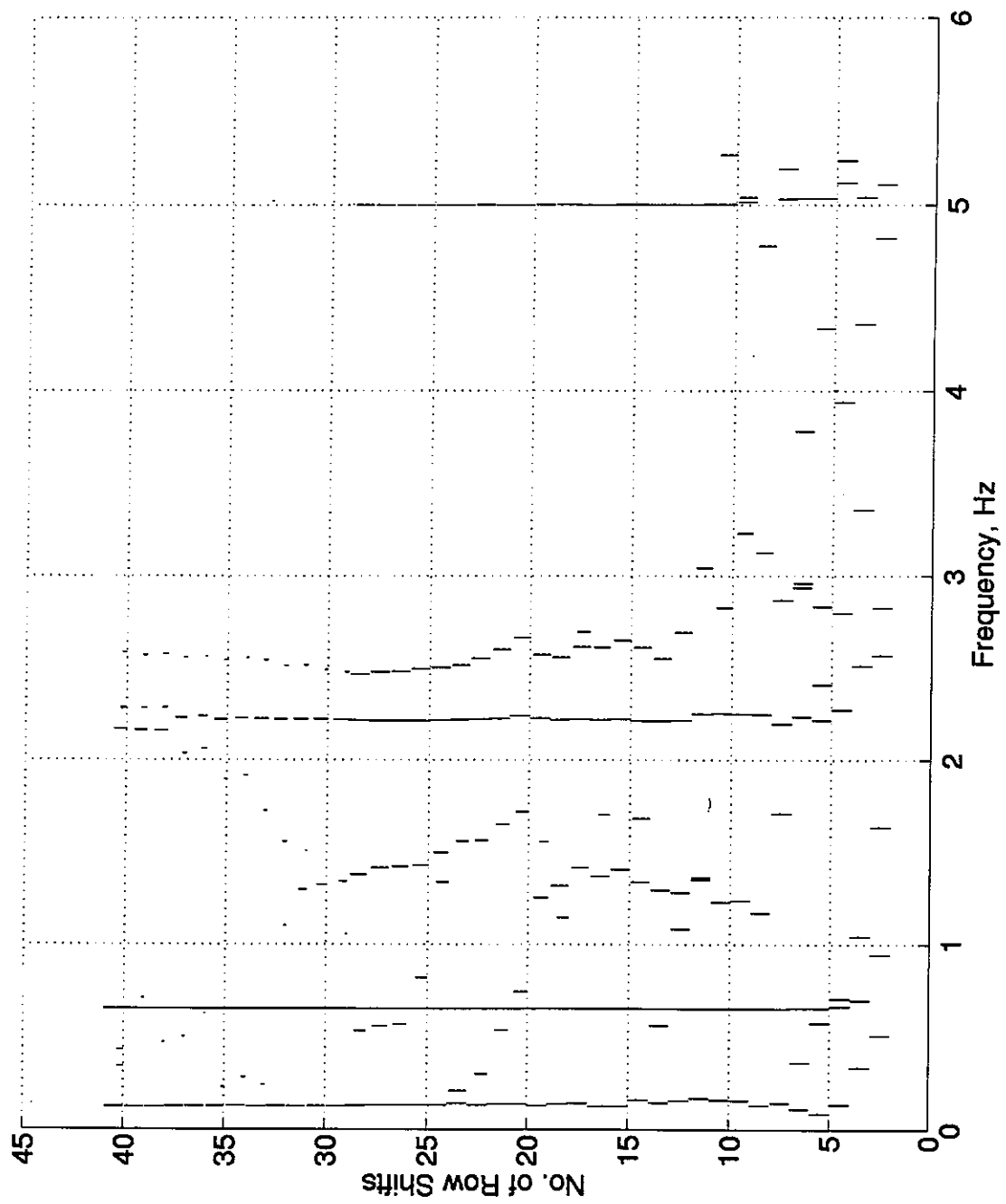


Figure 6.18: Modal Amplitude Coherence for Image Plane 4

of row shifts each of these modes exhibit high levels of confidence. However, each of these modes is present only in one of the cameras, indicating it is not a system mode but is particular to that image plane. This information can assist in determining sources of error in the measurements and isolating them if necessary. Also, modes can have high confidence levels in the image plane data and not have as high a level of confidence in the triangulated data. This is caused by the inclusion of noise in the data when the triangulation is done.

Once the modes are identified in the image plane, all of the camera data is analyzed together to assure coherence between the modes. The results of analyzing all of the image time series together is shown in Figure 6.19. It is *essential* to combine and analyze the image plane data so that the same frequency and damping values are used to reconstruct the image plane data. The reconstruction is done by selecting the system modes identified in the first step of the process and use the modal parameter values determined in the second step of the IPMA method.

As with the accelerometer and photogrammetric data, the results of the ERA analysis for the IPMA method is used to reconstruct the data and an example is shown in Figure 6.20. The data for each of the four cameras is reconstructed with the four most dominant modes. The reconstructed data is then used in the triangulation method to obtain new triangulated series for the targets. Then the ERA analysis is applied to this set of data and a plot of the MAC values at their corresponding frequencies is shown in Figure 6.21.

Comparing Figure 6.21 to Figure 6.9 shows that the three structural modes are much stronger in the reconstructed data. The image plane analysis allows the identification of modes that can be lost or not identified in the triangulated data. Also, it reduces noise and error modes from being passed on from the image plane to the global coordinate system.

As a comparison of the three methods, the frequencies and dampings for the three structural modes are presented in Table 6.2. The table demonstrates the strong agreement between the frequency values for all of the modes. There is some variation in the damping values but this variation is small and well within acceptable limits.

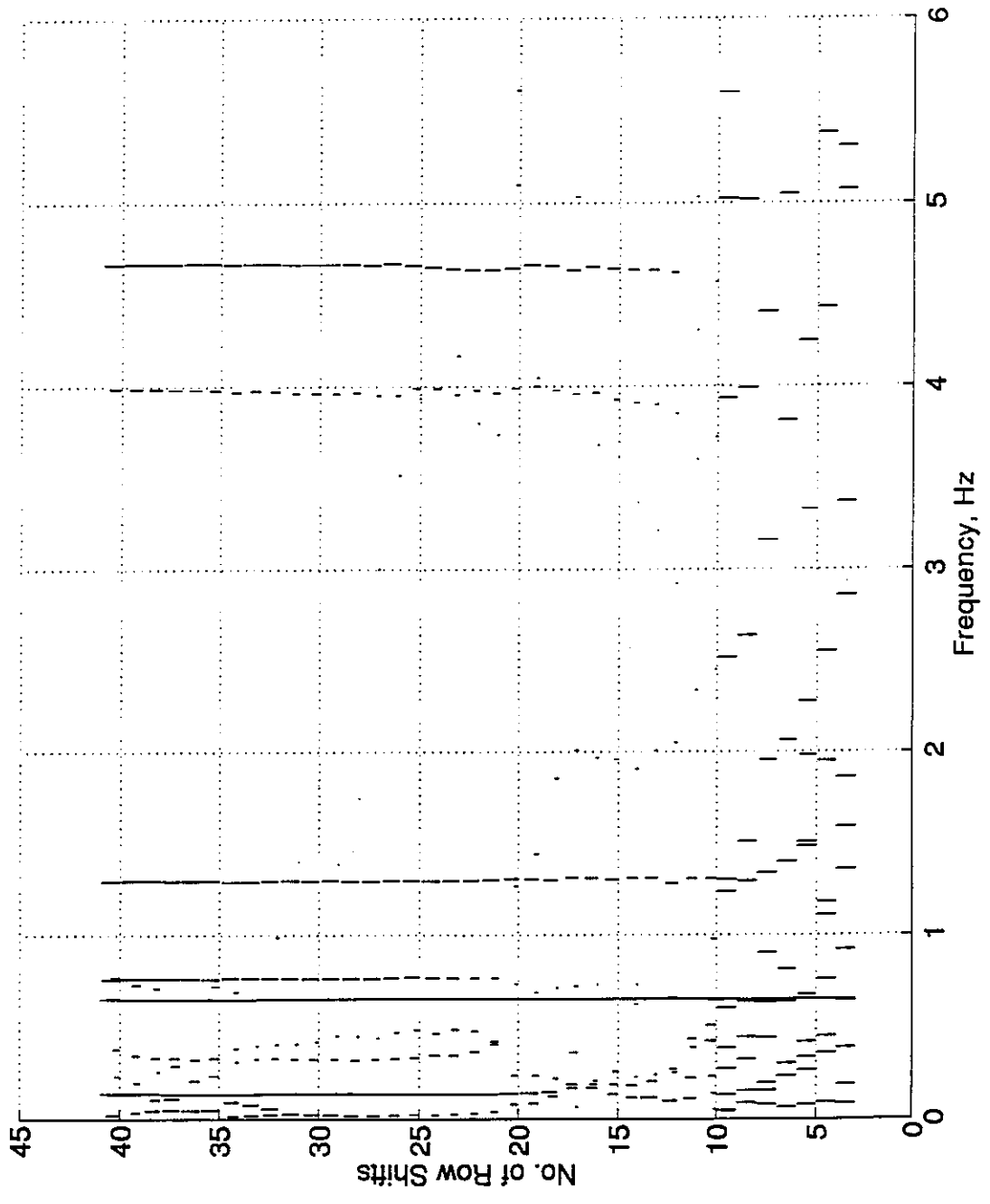


Figure 6.19: Modal Amplitude Coherence for All Image Plane Time Series

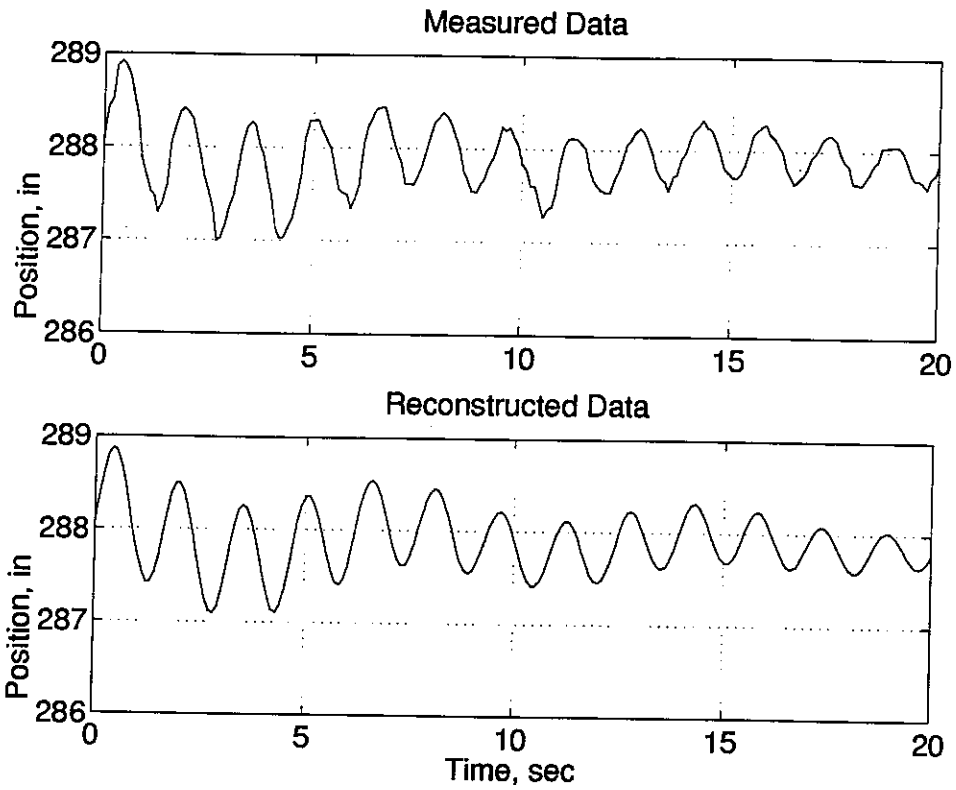


Table 6.2: Comparison of Frequency and Damping Results for Three Identification Methods

Method	First Bending Mode		Second Bending Mode		Coupling Mode	
	Freq.	Damp.	Freq.	Damp.	Freq.	Damp.
Accelerometer	0.65	1.29	0.76	0.41	1.31	0.5644
Photogrammetric	0.65	1.51	0.75	0.67	1.29	1.22
IPMA Method	0.65	1.43	0.75	0.80	1.30	2.53

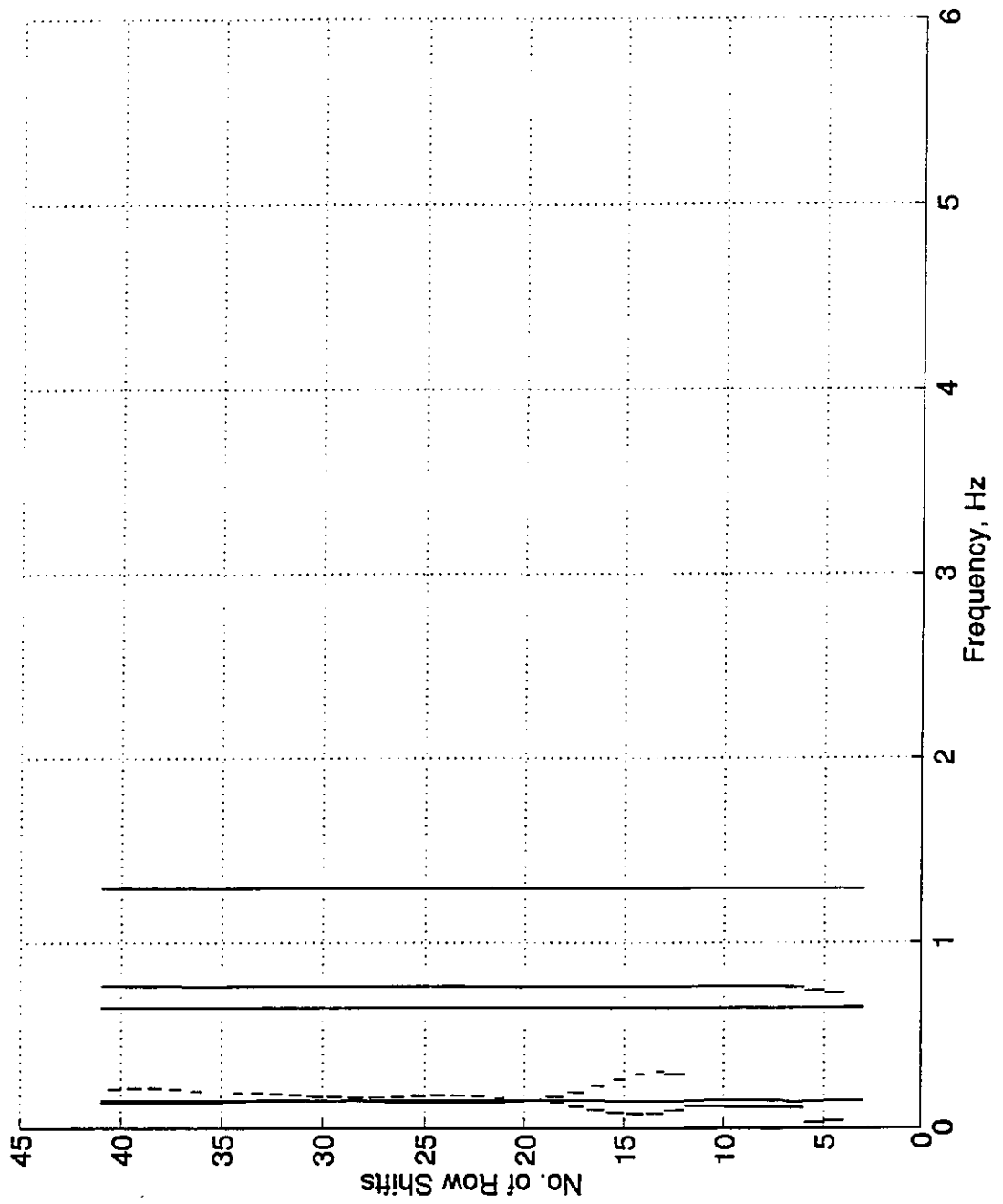


Figure 6.21: Modal Amplitude Coherence for Reconstructed Data

Table 6.3: Comparison of Modal Responses Near the Tip For Three Modes

Method	Mode 1	Mode 2	Mode 3
Accelerometer	0.347	0.201	0.0352
Photogrammetry	0.244	0.115	0.0265
IPMA Method	0.238	0.145	0.0265

Another method of comparison is to examine the mode shape response of the same point in all three methods. The modal response in the X direction of a point near the tip of the solar array due to each of the three structural modes are shown in Table 6.3. The table shows that most of the energy is in the first bending mode, and less energy is in the second bending mode and the the coupling mode. This important fact explains why only the first mode appears in all four image planes and the other two do not. It is important to remember that the input was designed to primarily excite the first mode. Another important comparison to make is the results from the IPMA method and the traditional photogrammetric method. These results are very similar for all three modes. This indicates the mode shapes response measured by the IPMA method are only slightly better than the traditional method but demonstrate that nothing is lost in the IPMA process. The reason both photogrammetric responses are smaller than the accelerometer response is the photogrammetric method does not have as high a resolution as the accelerometers.

Image plane analysis is beneficial in two ways. It can localize sources of error to individual cameras and allow the error to be filtered from the data before the triangulation. Second, the image plane information can indicate modes present that may not be identified after the least squares triangulation is completed.

# Chapter 7

## Conclusions

A method has been presented to assist in determining the dynamic characteristics of space structures. The Image Plane Analysis Method (IPMA) is designed to filter uncorrelated noise resulting from camera disturbances in photogrammetric data. IPMA first identifies structural modes and noise modes in the camera image plane before triangulating the data into an inertial coordinate system.

To evaluate this method, an experiment using the CEM3 testbed was performed to evaluate the IPMA method. Accelerometer measurements are used as a baseline for comparing the results from using the traditional photogrammetric method and the IPMA method. The accelerometer data analysis indicated three structural modes present, at 0.65 Hz, at 0.76 Hz, and at 1.31 Hz. The traditional photogrammetric method identified the first bending mode at 0.65 Hz, the second mode at 0.75 Hz and identified the coupling mode at 1.29 Hz. but the method did not adequately identify the bending mode at 0.75 Hz. The IPMA method identified all 3 structural modes. Also, the IPMA method demonstrated a slight improvement over the photogrammetric in measuring the modal response of the structure. Neither the photogrammetric or IPMA method matched the accelerometer results for the modal response of the structure, but this is due to the lower resolution associated with the photogrammetric measurements.

Several important considerations arose from the experiment. The placement of cameras with respect to the motion of the structure can affect the ability of the IPMA

method to detect motion due to certain modes. If the motion induced by a mode is orthogonal to the camera plane, it is more difficult to measure this motion. It is best to place the cameras where the motion of the structure is parallel to the image plane. The second consideration is the placement or selection of targets on the structure. If a target is placed at or near a node, and there are few other targets in the image, a particular mode may not appear strongly in the analysis of that image plane data. Since the IPMA method relies on the principle that all structural modes will appear in all cameras, some structural modes may be discarded.

It has been shown that the IPMA method improves identification results over the traditional photogrammetric method based on qualitative observation. This new method improves the standard photogrammetric method by identifying and removing noise contributions to the signals when the noise is a result of independent disturbances to the cameras. The IPMA method identifies structural modes in the image plane and differentiates them from local noise modes resulting from disturbances applied to the camera. Modes peculiar to only one camera are discarded and only modes that appear in two or more cameras are identified as structural modes. The image plane data is reconstructed using only the modal parameters identified as system parameters. Once the image plane data is reconstructed, the location of the points in object space are determined using the least-squares fit, similar to what is done in the traditional photogrammetric method.

# Appendix A

## Partial Derivatives of Collinearity Equations

First, define the variables  $U$ ,  $V$ , and  $W$  as

$$\begin{bmatrix} U \\ V \\ W \end{bmatrix} = M \begin{bmatrix} X - X_c \\ Y - Y_c \\ Z - Z_c \end{bmatrix} \quad (\text{A.1})$$

where  $M$  is the rotation matrix given by 2.2.

The partial derivatives of the equations with respect to the image coordinates are

$$\begin{bmatrix} \frac{\partial f_1}{\partial x} & \frac{\partial f_1}{\partial y} \\ \frac{\partial f_2}{\partial x} & \frac{\partial f_2}{\partial y} \end{bmatrix} = \begin{bmatrix} 1 & 0 \\ 0 & 1 \end{bmatrix} \quad (\text{A.2})$$

With respect to the camera interior orientation parameters

$$\begin{bmatrix} \frac{\partial f_1}{\partial x_p} & \frac{\partial f_1}{\partial y_p} & \frac{\partial f_1}{\partial c} \\ \frac{\partial f_2}{\partial x_p} & \frac{\partial f_2}{\partial y_p} & \frac{\partial f_2}{\partial c} \end{bmatrix} = \begin{bmatrix} -1 & 0 & U/W \\ 0 & -1 & V/W \end{bmatrix} \quad (\text{A.3})$$

Then, with respect to the camera position

$$\begin{aligned}
\frac{\partial f_1}{\partial X_c} &= \frac{c}{W} [-m_{11} + (U/W)m_{31}] \\
\frac{\partial f_1}{\partial Y_c} &= \frac{c}{W} [-m_{12} + (U/W)m_{32}] \\
\frac{\partial f_1}{\partial Z_c} &= \frac{c}{W} [-m_{13} + (U/W)m_{33}] \\
\frac{\partial f_2}{\partial X_c} &= \frac{c}{W} [-m_{21} + (V/W)m_{31}] \\
\frac{\partial f_2}{\partial Y_c} &= \frac{c}{W} [-m_{22} + (V/W)m_{32}] \\
\frac{\partial f_2}{\partial Z_c} &= \frac{c}{W} [-m_{23} + (V/W)m_{33}]
\end{aligned} \tag{A.4}$$

And finally, with respect to the exterior camera parameters (see Chapter 2 for definitions)

$$\begin{aligned}
\frac{\partial f_1}{\partial \omega} &= \frac{c}{W} \left( m_{12}(Z - Z_c) - m_{13}(Y - Y_c) - \frac{U}{W} [m_{32}(Z - Z_c) - m_{33}(Y - Y_c)] \right) \\
\frac{\partial f_1}{\partial \phi} &= \frac{c}{W} \left( -\cos \kappa W - \frac{U}{W} [\cos \kappa U - \sin \kappa V] \right) \\
\frac{\partial f_1}{\partial \omega} &= \frac{cV}{W} \\
\frac{\partial f_2}{\partial \omega} &= \frac{c}{W} \left( m_{22}(Z - Z_c) - m_{23}(Y - Y_c) - \frac{V}{W} [m_{32}(Z - Z_c) - m_{33}(Y - Y_c)] \right) \\
\frac{\partial f_2}{\partial \phi} &= \frac{c}{W} \left( \sin \kappa W - \frac{V}{W} [\cos \kappa U - \sin \kappa V] \right) \\
\frac{\partial f_2}{\partial \omega} &= \frac{-cU}{W}
\end{aligned} \tag{A.5}$$

The partial derivatives with respect to the point coordinates are the negatives of the partial derivatives with respect to the camera coordinates.

# Appendix B

## Accelerometer Time Series

The accelerometer time histories are given in this appendix. All accelerations are measured in  $in/s^2$ . The key for the 24 plots is given below (the number in parenthesis is the corresponding grid point for the finite element model of the testbed):

- 1) Y direction, located at solar array base plate(2329).
- 2) Z direction, located at solar array base plate(2329).
- 3) X direction, located at solar array base plate(2329).
- 4) Z direction, located 9 in. back from tip(600202).
- 5) X direction, located 9 in. back from tip(600202).
- 6) Y direction, located 9 in. back from tip(600202).
- 7) Z direction, located at solar array tip(600203).
- 8) X direction, located at solar array tip(600203).
- 9) Z direction, located 26 in. back from tip(600181).
- 10) X direction, located 26 in. back from tip(600181).
- 11) Z direction, located 52 in. back from tip(600151).
- 12) X direction, located 52 in. back from tip(600151).

- 13) Z direction, located 107 in. back from tip(600091).
- 14) X direction, located 107 in. back from tip(600091).
- 15) Y direction, located 107 in. back from tip(600091).
- 16) X direction, located 107 in. back from tip(600092).
- 17) Z direction, located 107 in. back from tip(600092).
- 18) Z direction, located 134 in. back from tip(600061).
- 19) X direction, located 134 in. back from tip(600061).
- 20) X direction, located 162 in. back from tip(600031).
- 21) Z direction, located 162 in. back from tip(600031).
- 22) X direction, located 80 in. back from tip(600121).
- 23) Z direction, located 80 in. back from tip(600121).
- 24) Y direction, located on the truss of the structure(2301).

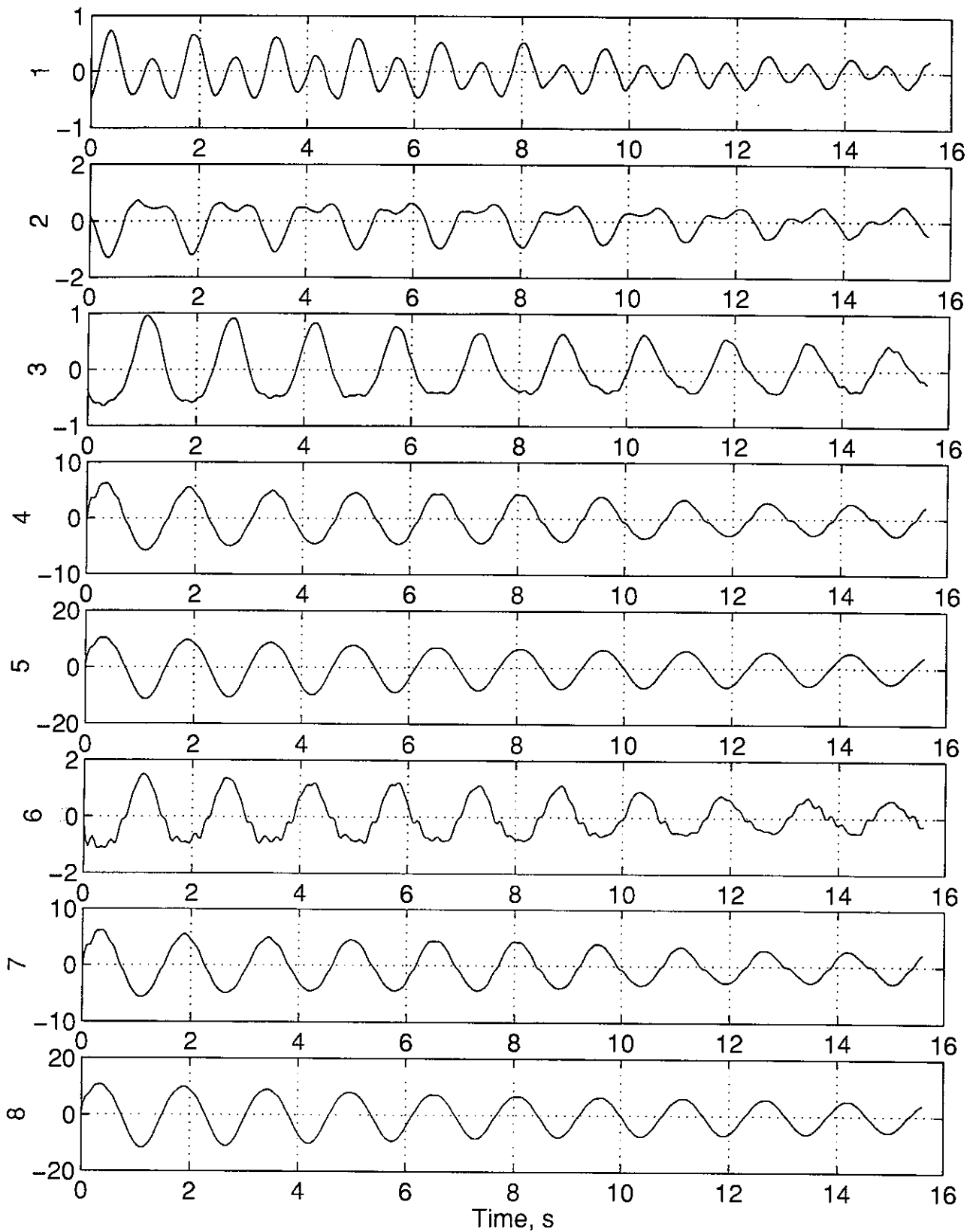


Figure B.1: Accelerometer Time Series # 1-8

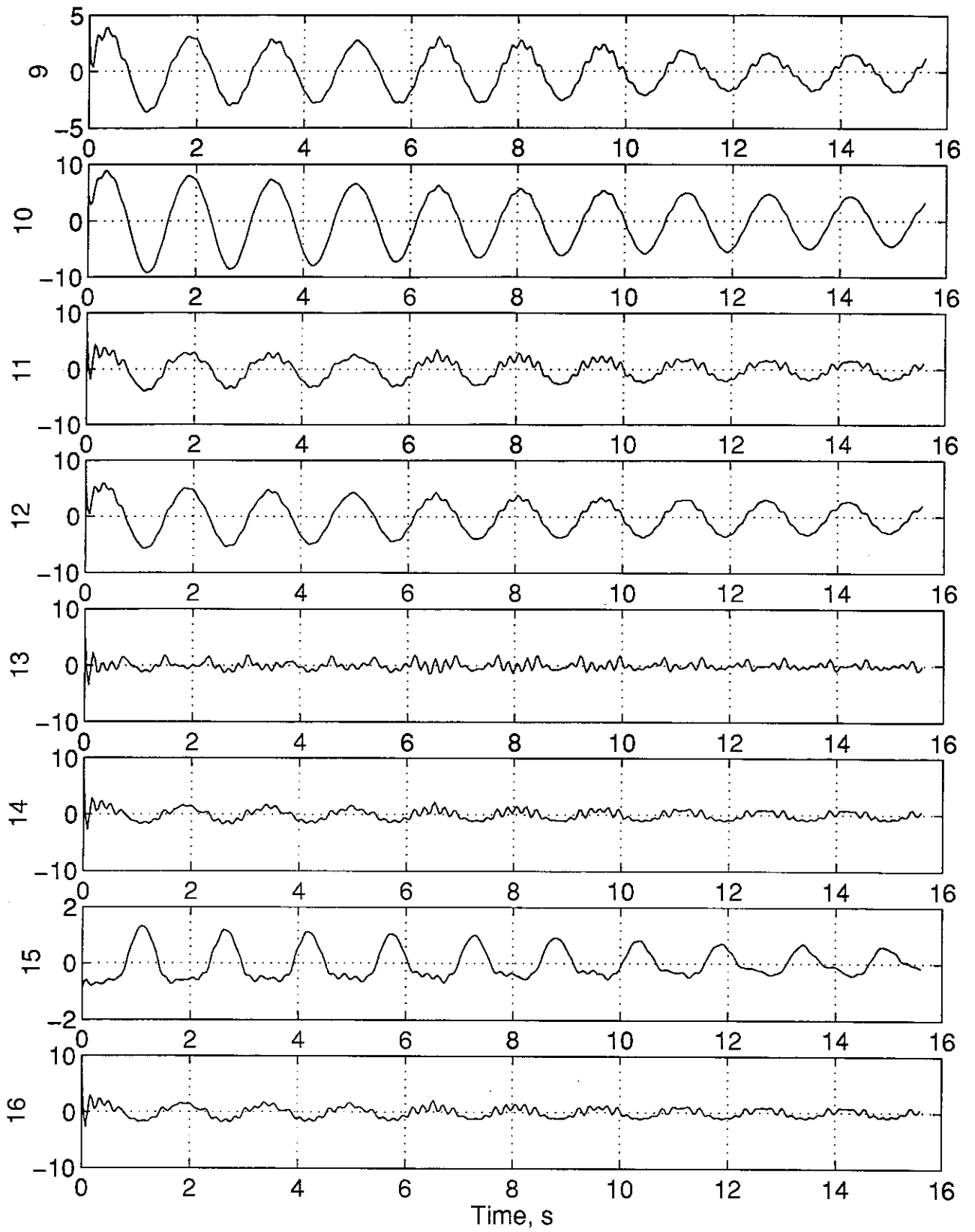


Figure B.2: Accelerometer Time Series # 9-16

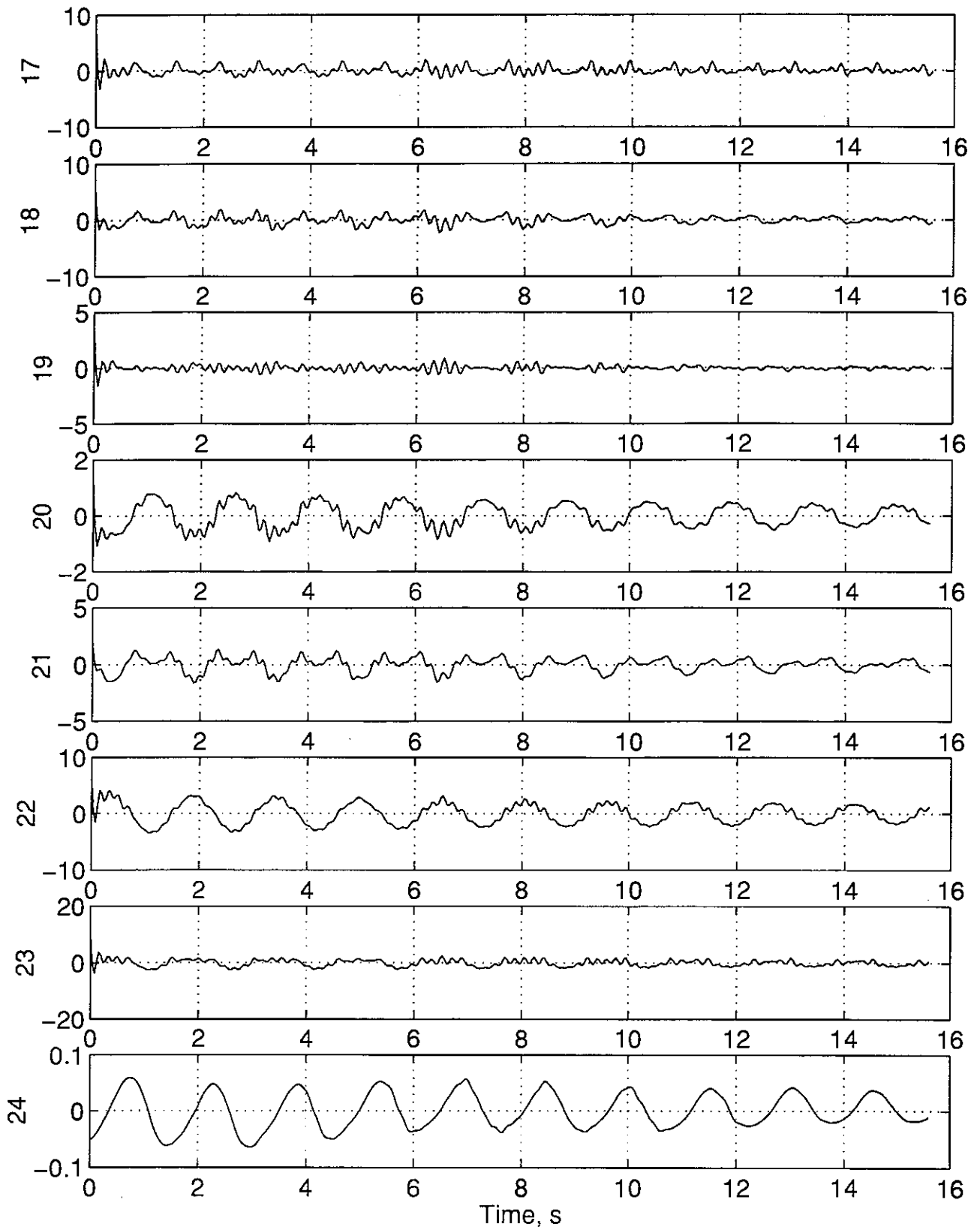


Figure B.3: Accelerometer Time Series # 17-24

## Appendix C

# Triangulated Targets' Time Series

The triangulated time series of the structure targets are presented in this appendix.

- 1) Series 1 through 8, Targets 1-8, X position in global coordinates.
- 2) Series 9 through 16, Targets 1-8, Y position in global coordinates.
- 3) Series 17 through 24, Targets 1-8, Z position in global coordinates.

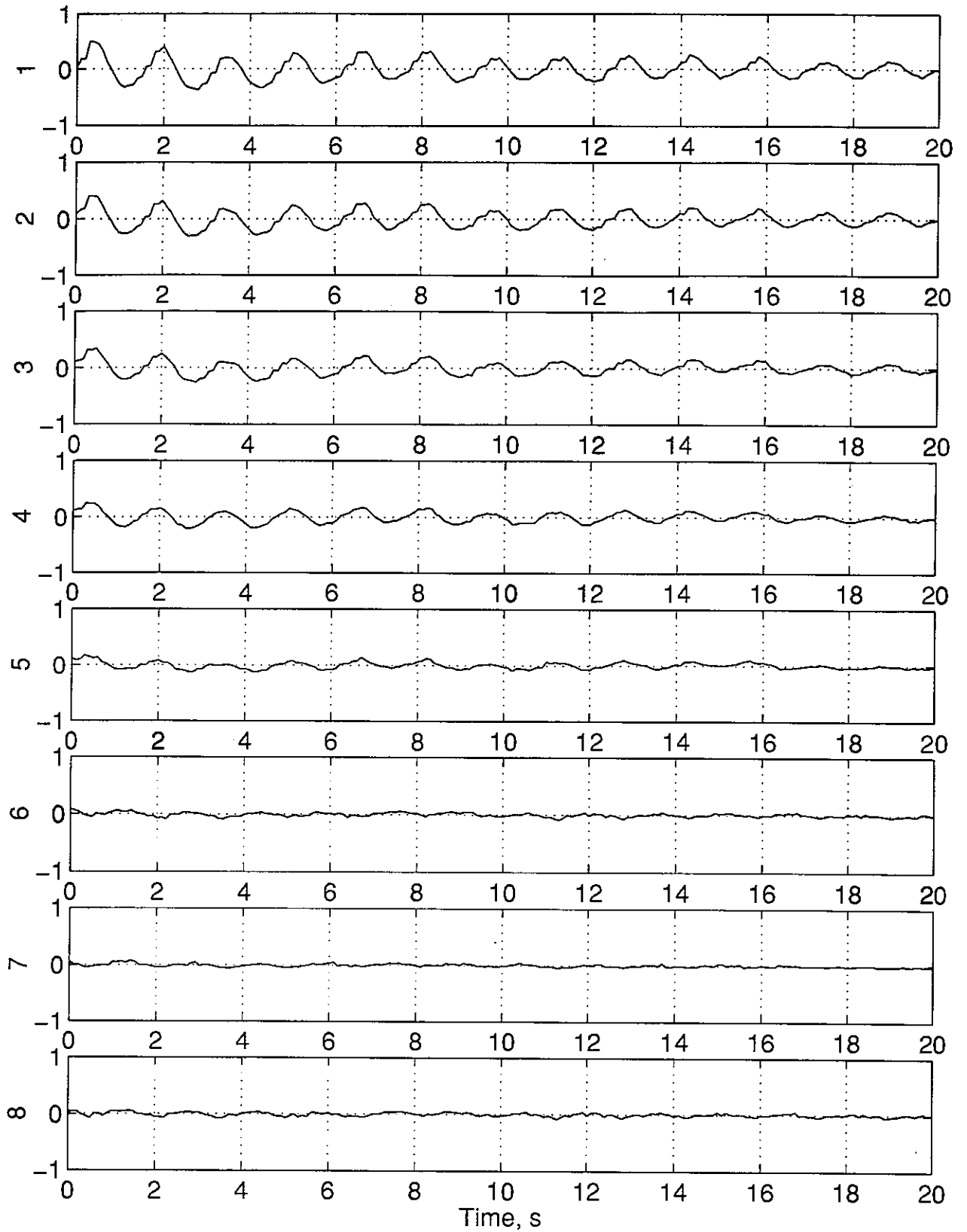


Figure C.1: Triangulated Time Series # 1-8

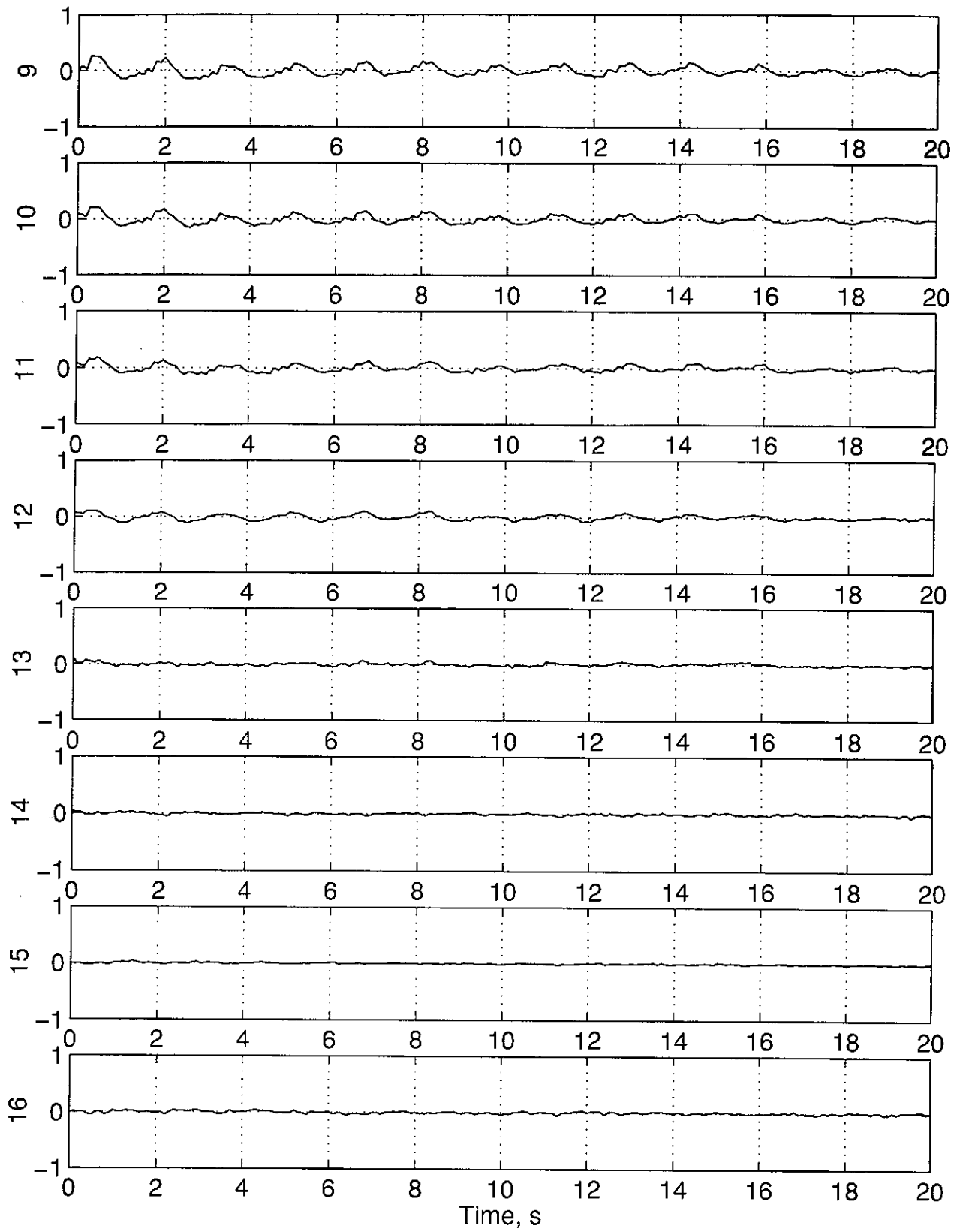


Figure C.2: Triangulated Time Series # 9-16

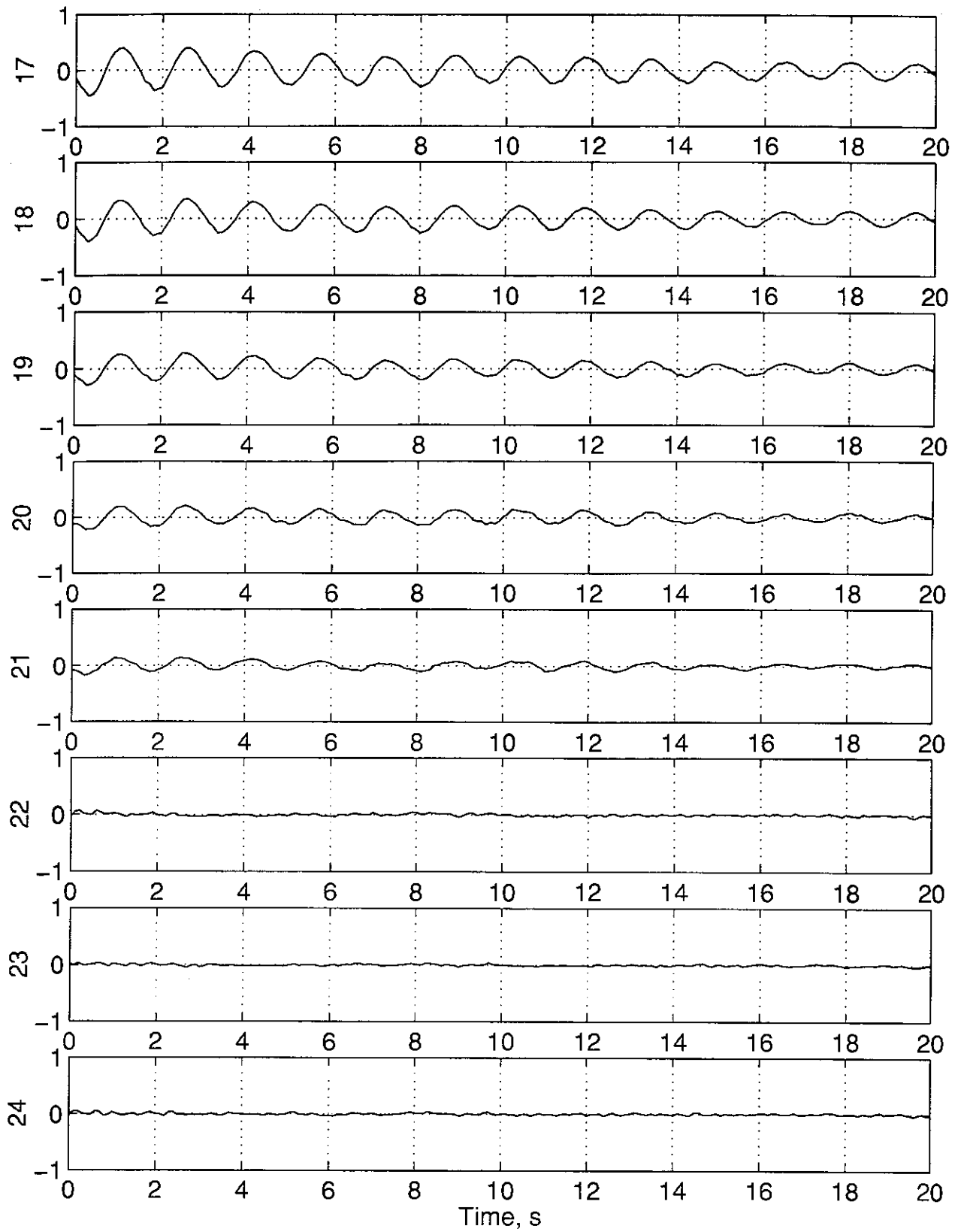


Figure C.3: Triangulated Time Series # 17-24

## Appendix D

### Image Plane Targets' Time Series

The image plane time histories are given in this appendix. The key for each image plane is given below:

Image Plane 1:

- 1) Series 1 through 5, Targets 1-5, X position in image plane coordinates.
- 2) Series 6 through 10, Targets 1-5, Y position in image plane coordinates.

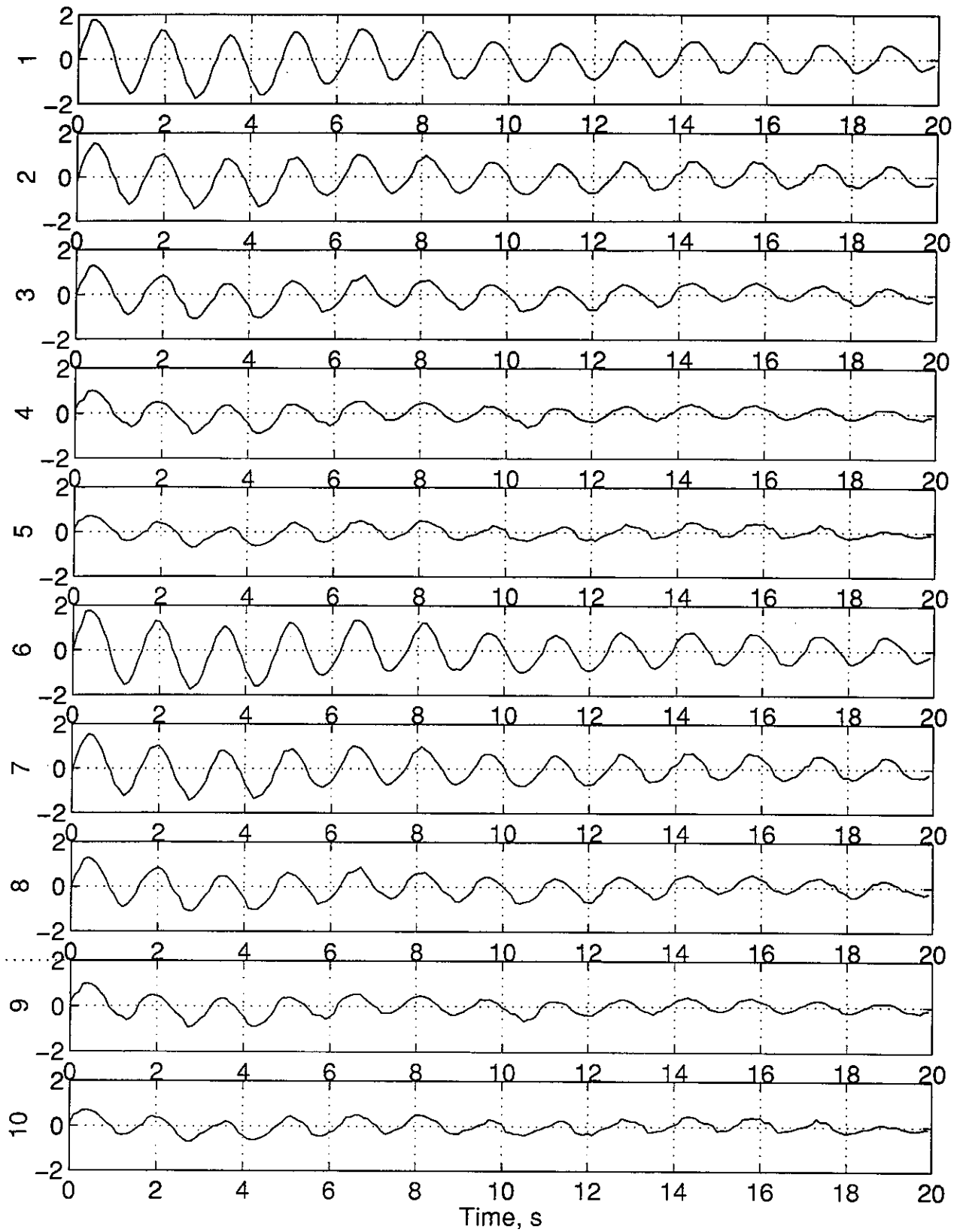


Figure D.1: Image Plane # 1 Time Series

Image Plane 2:

- 1) Series 1 through 5, Targets 1-5, X position in image plane coordinates.
- 2) Series 6 through 10, Targets 1-5, Y position in image plane coordinates.

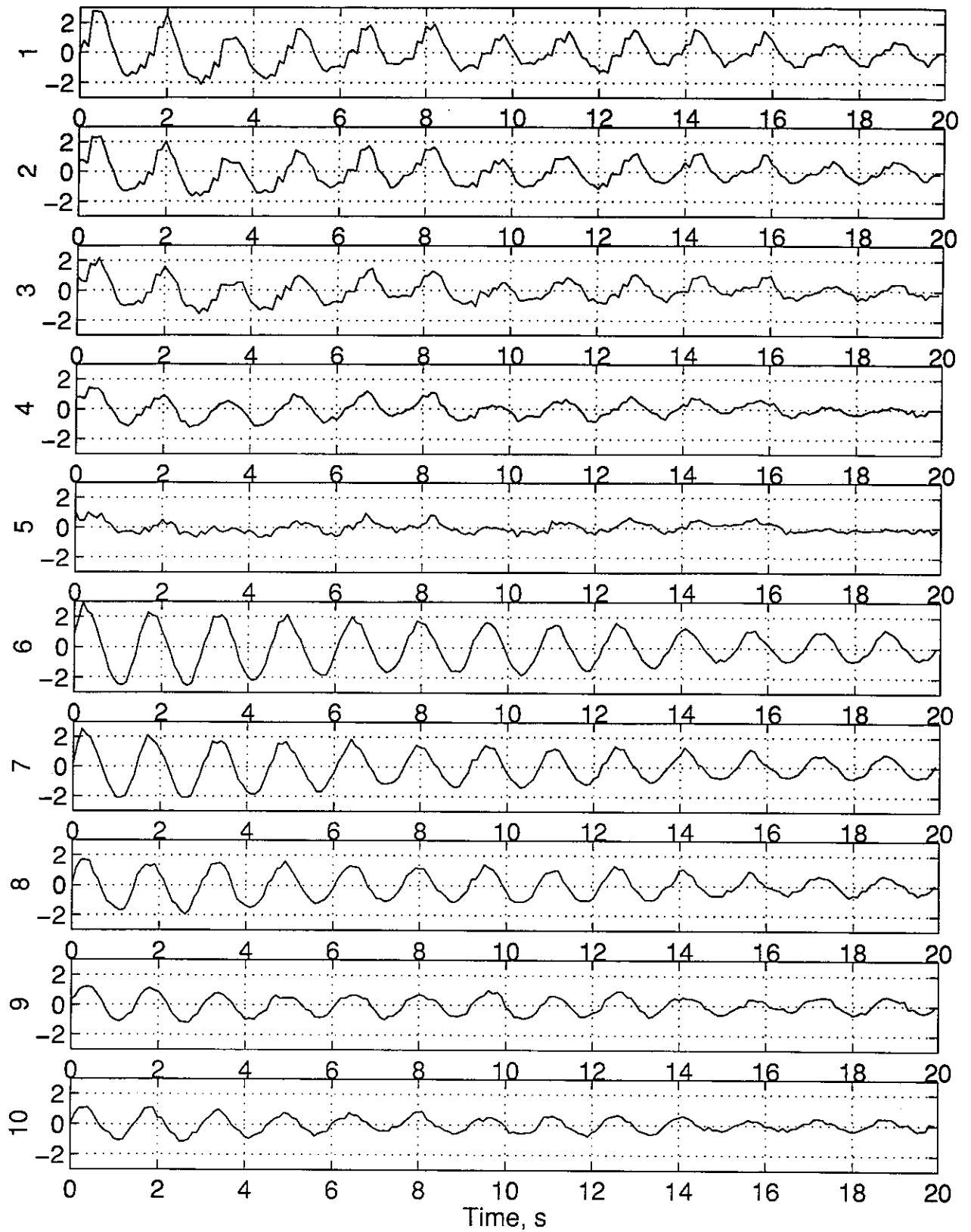


Figure D.2: Image Plane # 2 Time Series

Image Plane 3:

- 1) Series 1 through 3, Targets 6-8, X position in image plane coordinates.
- 2) Series 4 through 6, Targets 6-8, Y position in image plane coordinates.

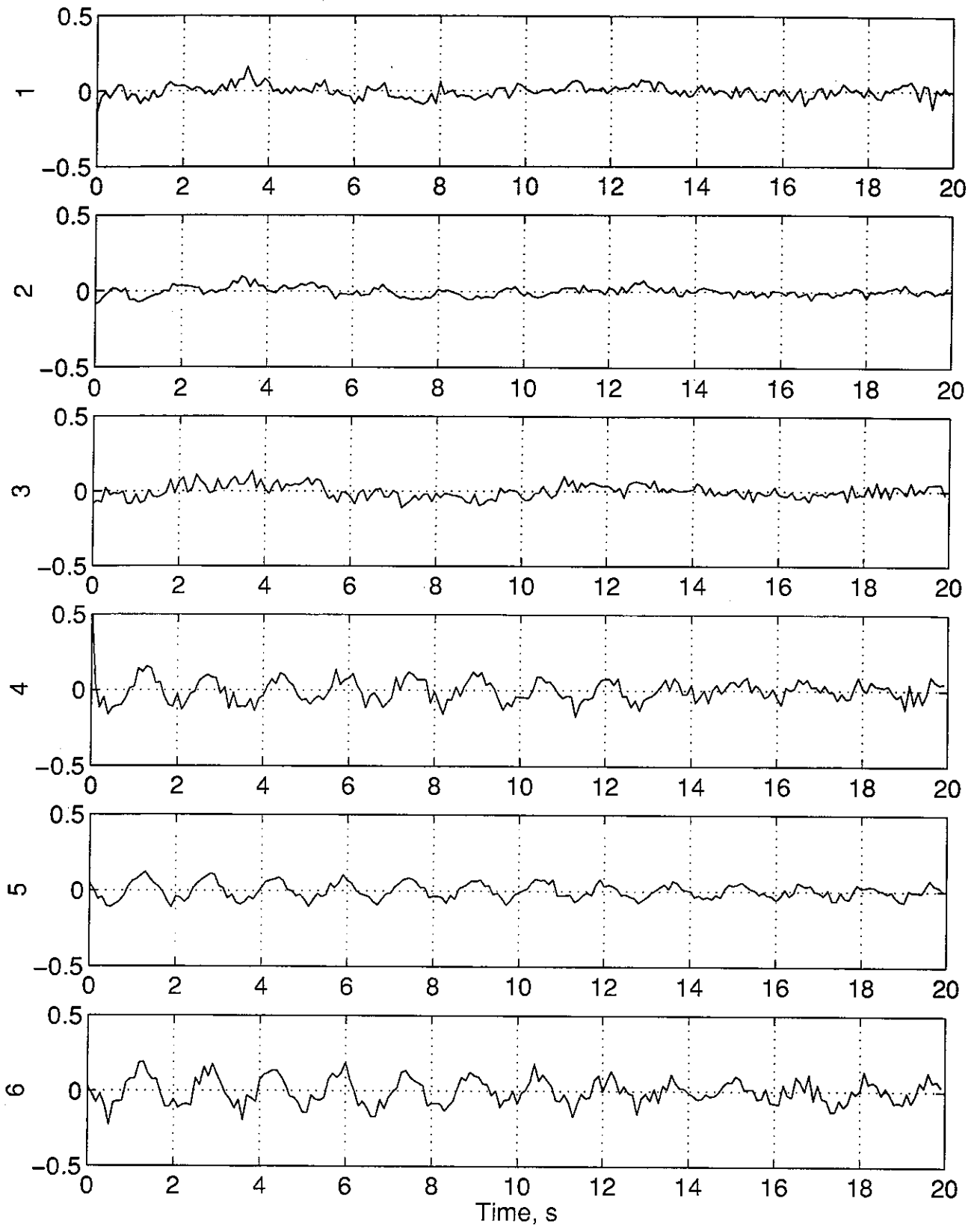


Figure D.3: Image Plane # 3 Time Series

Image Plane 4:

- 1) Series 1 through 3, Targets 6-8, X position in image plane coordinates.
- 2) Series 4 through 6, Targets 6-8, Y position in image plane coordinates.

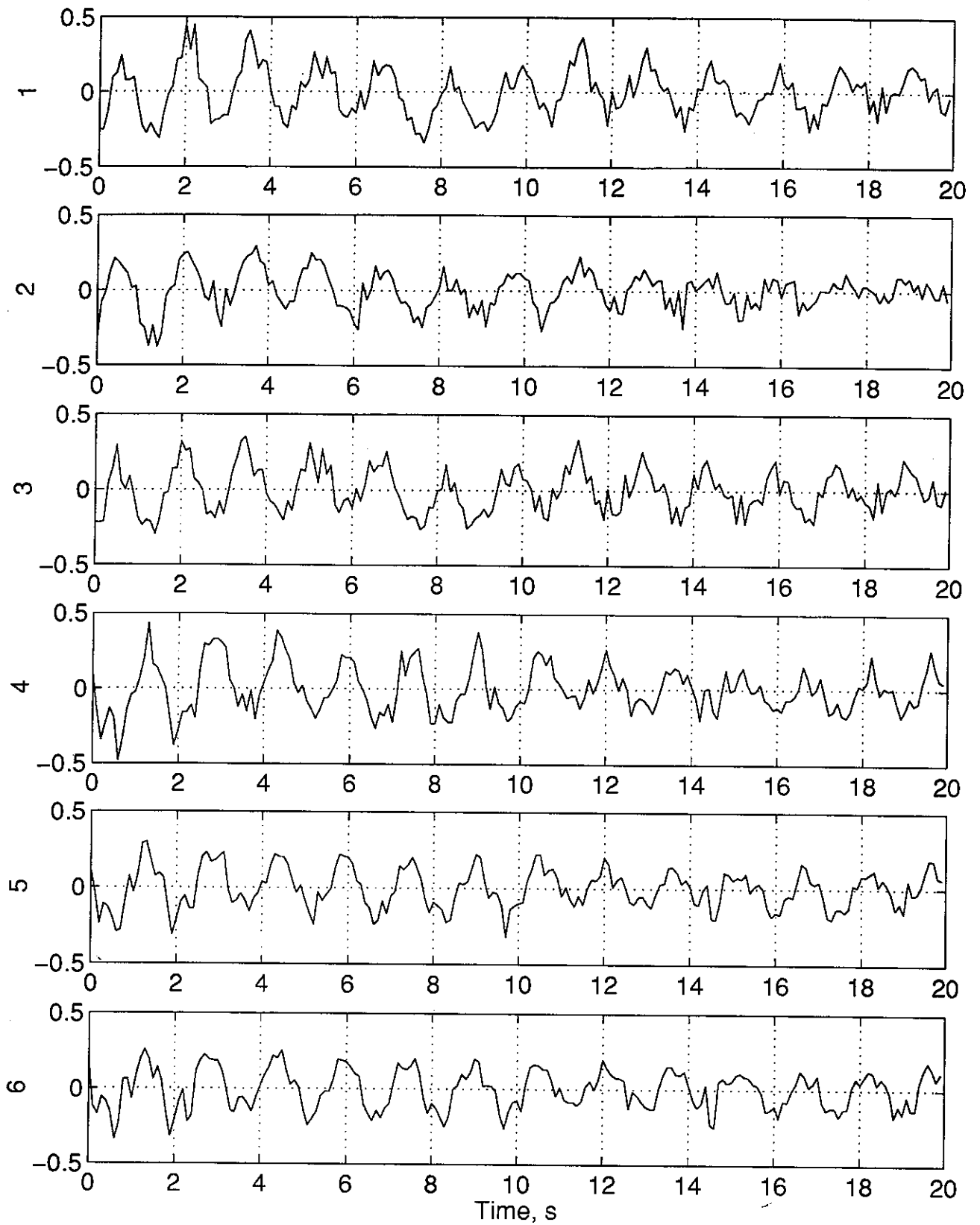


Figure D.4: Image Plane # 4 Time Series

# Bibliography

- [1] Gilbert, M.G., Welch, S.S., and Moore, C.L., "The Photogrammetric Appendage Structural Dynamics Experiment," NASA cp-3310, Sept. 1995.
- [2] W. L. Poston "Optimal Sensor Locations for On-orbit Modal Identification of Large Space Structures." Master's Thesis, George Washington University, 1989.
- [3] Nesman, T.E., and Reed, D.K., "SAFE/DAE: Modal test in Space," NASA S7N20584, August 1986.
- [4] Methley, B.D.F., *Computational Models in Surveying and Photogrammetry*, Blackie & Sons Ltd., Glasgow, Scotland, 1986.
- [5] Brown, D.C., "Application of Close-Range Photogrammetry to Measurements of Structures in Orbit", Volume 1, Final Report, Sept. 1980.
- [6] Slama, C.C., *Manual of Photogrammetry*, American Society of Photogrammetry, Falls Church, Virginia, 1980.
- [7] Brown, D.C.. "Application of Close-Range Photogrammetry to Measurements of Structures in Orbit". Volume 2, Final Report, Sept. 1980.
- [8] Karara, H.M., *Non-Topographic Photogrammetry*, 2nd ed., American Society for Photogrammetry and Remote Sensing, Falls Church, Virginia, 1989.
- [9] Juang, J.-N., *Applied System Identification*, Prentice Hall PTR, Englewoods Cliff, New Jersey, 1994.

- [10] Papadopoulos, M., and Tolson, R.H., "System Identification for Space Station Freedom Using Observer/Kalman Filter Markov Parameters", NASA Contract Report 191521, August, 1993.
- [11] Juang, J., and Pappa, R.S., "An Eigensystem Realization Algorithm for Modal Parameter Identification and Model Reduction," *Journal on Guidance*, Vol. 8, No. 5, Sept.-Oct. 1985, pp. 620-627.
- [12] Juang, S.Z., "Equivalents of Some System Identification Methods That Use Finite Hankel Matrices," M.S. Thesis, Dept. of Civil, Mechanical, and Environmental Engineering, George Washington University, Hampton, VA, March 1992.
- [13] West, G.A.W. and Clarke, T.A., "A Survey and Examination of Subpixel Measurement Techniques," *Proceedings of the Society of Photo-Optical Instrumentation Engineers*, Vol. 1395, Sept. 1990, pp. 456-463.
- [14] Gronet, M.J., Davis, D.A., and Tan, M.K., "Development of the CSI Phase-3 Evolutionary Model Testbed," NAS1-19241, Oct. 1994.
- [15] Pappa, R.S., Elliot, K. B., and Schenk, A., "Consistent-Mode Indicator for the Eigensystem Realization Algorithm." *Journal of Guidance, Control, and Dynamics*, Vol. 16, No. 5, Sept.-Oct. 1993, pp. 852-858.